



HAL
open science

Ionization fraction and the enhanced sulfur chemistry in Barnard 1

A. Fuente, J. Cernicharo, E. Roueff, M. Gerin, J. Pety, N. Marcelino, R.
Bachiller, B. Lefloch, O. Roncero, A. Aguado

► **To cite this version:**

A. Fuente, J. Cernicharo, E. Roueff, M. Gerin, J. Pety, et al.. Ionization fraction and the enhanced sulfur chemistry in Barnard 1. *Astronomy and Astrophysics - A&A*, 2016, 593, pp.A94. 10.1051/0004-6361/201628285 . hal-02317813

HAL Id: hal-02317813

<https://hal.science/hal-02317813>

Submitted on 27 Mar 2024

HAL is a multi-disciplinary open access archive for the deposit and dissemination of scientific research documents, whether they are published or not. The documents may come from teaching and research institutions in France or abroad, or from public or private research centers.

L'archive ouverte pluridisciplinaire **HAL**, est destinée au dépôt et à la diffusion de documents scientifiques de niveau recherche, publiés ou non, émanant des établissements d'enseignement et de recherche français ou étrangers, des laboratoires publics ou privés.

Published in final edited form as:

Astron Astrophys. 2016 September ; 593: . doi:10.1051/0004-6361/201628285.

Ionization fraction and the enhanced sulfur chemistry in Barnard

1

A. Fuente¹, J. Cernicharo², E. Roueff^{3,4}, M. Gerin^{3,4}, J. Pety⁵, N. Marcelino⁶, R. Bachiller¹, B. Lefloch⁷, O. Roncero⁸, and A. Aguado⁹

¹Observatorio Astronómico Nacional (OAN,IGN), Apdo 112, E-28803 Alcalá de Henares (Spain) a.fuente@oan.es

²Instituto de Ciencia de Materiales de Madrid, ICMM-CSIC, C/ Sor Juana Inés de la Cruz 3, E-28049 Cantoblanco, Spain

³CNRS UMR 8112, LERMA, Observatoire de Paris and École Normale Supérieure. 24 rue Lhomond, 75231 Paris Cedex 05, France

⁴Sorbonne Universités, UPMC Univ. Paris 06, UMR8112, LERMA, F-75005 Paris, France

⁵Institut de Radioastronomie Millimétrique, 300 Rue de la Piscine, F-38406 Saint Martin d'Hères, France

⁶INAF, Osservatorio di Radioastronomia, via P. Gobetti 101, I-40129, Bologna, Italy

⁷Institut de Planétologie et d'Astrophysique de Grenoble (IPAG) UMR 5274, Université UJF-Grenoble 1/CNRS-INSU, F-38041 Grenoble, France

⁸Instituto de Física Fundamental (IFF-CSIC), C.S.I.C., Serrano 123, E-28006 Madrid, Spain

⁹Facultad de Ciencias, Unidad Asociada de Química-Física Aplicada CSIC-UAM, Universidad Autónoma de Madrid, E-28049 Madrid, Spain

Abstract

Context—Barnard B1b has revealed as one of the most interesting globules from the chemical and dynamical point of view. It presents a rich molecular chemistry characterized by large abundances of deuterated and complex molecules. Furthermore, it hosts an extremely young Class 0 object and one candidate to First Hydrostatic Core (FHSC) proving the youth of this star forming region.

Aims—Our aim is to determine the cosmic ray ionization rate, ζ_{H_2} , and the depletion factors in this extremely young star forming region. These parameters determine the dynamical evolution of the core.

Methods—We carried out a spectral survey towards Barnard 1b as part of the IRAM Large program ASAI using the IRAM 30-m telescope at Pico Veleta (Spain). This provided a very complete inventory of neutral and ionic C-, N- and S- bearing species with, up to our knowledge, the first secure detections of the deuterated ions DCS⁺ and DOCO⁺. We use a state-of-the-art pseudo-time-dependent gas-phase chemical model that includes the ortho and para forms of

H_2 , H_2^+ , D_2^+ , H_3^+ , H_2D^+ , D_2H^+ , D_2 and D_3^+ to determine the local value of the cosmic ray ionization rate and the depletion factors.

Results—Our model assumes $n(\text{H}_2)=10^5 \text{ cm}^{-3}$ and $T_k=12 \text{ K}$, as derived from our previous works. The observational data are well fitted with ζ_{H_2} between $3 \times 10^{-17} \text{ s}^{-1}$ and 10^{-16} s^{-1} , and the following elemental abundances: $\text{O}/\text{H}=3 \times 10^{-5}$, $\text{N}/\text{H}=6.4\text{--}8 \times 10^{-5}$, $\text{C}/\text{H}=1.7 \times 10^{-5}$ and S/H between 6.0×10^{-7} and 1.0×10^{-6} . The large number of neutral/protonated species detected, allows us to derive the elemental abundances and cosmic ray ionization rate simultaneously. Elemental depletions are estimated to be ~ 10 for C and O, ~ 1 for N and ~ 25 for S.

Conclusions—Barnard B1b presents similar depletions of C and O than those measured in pre-stellar cores. The depletion of sulfur is higher than that of C and O but not as extreme as in cold cores. In fact, it is similar to the values found in some bipolar outflows, hot cores and photon-dominated regions. Several scenarios are discussed to account for these peculiar abundances. We propose that it is the consequence of the initial conditions (important outflows and enhanced UV fields in the surroundings) and a rapid collapse ($\sim 0.1 \text{ Myr}$) that permits to maintain most S- and N-bearing species in gas phase to great optical depths. The interaction of the compact outflow associated with B1b-S with the surrounding material could enhance the abundances of S-bearing molecules, as well.

Keywords

astrochemistry; stars:formation; ISM: molecules; ISM: individual (Barnard 1)

1 Introduction

Cosmic rays (hereafter CRs) play a leading role in the chemistry, heating and dynamics of the interstellar medium (ISM). CRs interact with dense molecular clouds by ionizing their main component, the molecular hydrogen, and this process initiates a series of ion-molecule reactions that form compounds of increasing complexity to eventually build up the rich chemistry observed in dark clouds (see e.g. Wakelam et al., 2010). CRs also represent an important heating source for molecular clouds. Collisions with interstellar molecules and atoms convert about half of the energy of primary and secondary electrons yielded by the ionization process into heat (Glassgold & Langer, 1973; Glassgold et al., 2012). Finally, the ionization fraction controls the coupling of magnetic fields with the gas, driving the dissipation of turbulence and angular momentum transfer, thus playing a crucial role in protostellar collapse and the dynamics of accretion discs (see Padovani et al., 2013 and references therein).

The cosmic-ray ionization rate ζ_{H_2} is the number of hydrogen molecule ionization per second produced by CRs. In absence of other ionization agents (X-rays, UV photons, J-type shocks), the ionization fraction is proportional to $\sqrt{\zeta_{\text{H}_2}}$ that becomes the key parameter in the molecular cloud evolution (McKee, 1989; Caselli et al., 2002). During the last 50 years, values of ζ_{H_2} ranging from a few 10^{-18} s^{-1} to a few 10^{-16} s^{-1} have been observationally determined in diffuse and dense interstellar clouds (Galli & Padovani 2015, and references therein). The cosmic ray ionization rate has usually been estimated from the $[\text{HCO}^+]/[\text{CO}]$

and/or $[\text{DCO}^+]/[\text{HCO}^+]$ abundance ratios using simple analytical expressions (e.g. Guelin et al., 1977; Wootten et al., 1979; Dalgarno & Lepp, 1984). In recent studies, these estimates have been improved by using comprehensive chemistry models (Caselli et al., 1999; Bergin et al., 1999). These models show that the gas ionization fraction is also dependent on the depletion factors that should be known to accurately estimate ζ_{H_2} (Caselli et al., 1999).

Chemical modeling is required to constrain the elemental abundances and the cosmic ray ionization rate. We carried out a spectral survey towards Barnard 1b as part of the IRAM Large program ASAI using the IRAM 30-m telescope at Pico Veleta (Spain) which provided a very complete inventory of ionic species including C-, N- and S-bearing compounds. The large number of neutral/protonated species allows us to derive the elemental abundances in gas phase and the cosmic ray ionization rate simultaneously, avoiding the uncertainty due to the unknown depletion factors in the latter.

1.1 Barnard 1

Barnard 1 (B1) belongs to the Perseus molecular cloud complex ($D=235$ pc). The Barnard 1 dark cloud itself is subdivided into several dense cores at different evolutionary stages of star formation. While B1-a and B1-c are known to host class 0 sources associated with high velocity outflows (Hatchell et al., 2005, 2007), the B1-b core appears to be more quiet, although its western edge is interacting with an outflow possibly arising from sources B1-a or B1-d, both located $1'$ SW of B1-b (see a sketch in Fig. 1).

The B1b region was mapped in many molecular tracers, e.g. HCO^+ , CS, NH_3 , ^{13}CO (Bachiller & Cernicharo, 1984; Bachiller et al., 1990), N_2H^+ (Huang & Hirano, 2013), H^{13}CO^+ (Hirano et al., 1999), or CH_3OH (Hiramatsu et al., 2010; Öberg et al., 2010). Interferometric observations of Barnard 1b revealed that this compact core hosts two young stellar objects (YSOs), B1b-N and B1b-S (Huang & Hirano, 2013), and a third more evolved source, hereafter B1b-W, with deep absorption from ices (Jørgensen et al., 2006). The two first sources are deeply embedded in the surrounding protostellar envelope, that seems essentially unaffected by the embedded sources as shown by the large column density, $N(\text{H}_2)\sim 7.6\times 10^{22}$ cm^2 (Daniel et al., 2013) and cold kinetic temperature, $T_K = 12$ K (Lis et al., 2010). Based on the Herschel fluxes and the subsequent SED modeling, Pezzuto et al. (2012) concluded that B1b-N and B1b-S were younger than Class 0 sources and proposed them as First Hydrostatic Core (FHSC) candidates. Using NOEMA, Gerin et al. (2015) obtained high resolution maps of the protostellar outflows and their envelope, confirming the young ages of B1b-N and B1b-S (~ 1000 yr and ~ 3000 yr), and the high density of the surrounding core (\sim a few 10^5 cm^{-3} for the outflowing gas).

From the chemical point of view, B1b is characterized by a rich chemistry. Indeed, many molecules were observed for the first time in this object, like HCNO (Marcelino et al., 2009) or CH_3O (Cernicharo et al., 2012). Additionally, B1b shows a high degree of deuterium fractionation and has been associated with first detections of multiply deuterated molecules, such as ND_3 (Lis et al., 2002) or D_2CS (Marcelino et al., 2005), consistent with the expected chemistry in a dense and cold core.

2 Observations

We carried out a spectral survey towards Barnard B1b ($\alpha_{J2000}=03^{\text{h}} 33^{\text{m}} 20.8^{\text{s}}$, $\delta_{J2000}=31^{\circ} 07' 34''.0$) using the IRAM 30-m telescope at Pico Veleta (Spain). This position is in between the two FHSC candidates B1b-N and B1b-S. The two protostellar cores lie inside the HPBW of the 30m telescope at 3mm, but they are missed at 1mm wavelengths (see Fig. 2).

The 3mm observations were performed between January and May 2012 (see Cernicharo et al., 2012), which used the narrow mode of the FTS allowing a higher spectral resolution of 50 kHz. The observing mode in this case was frequency switching with a frequency throw of 7.14 MHz, which removes standing waves between the secondary and the receivers. Several observing periods were scheduled on July and February 2013 and January and March 2014, to cover the 1 and 2 mm bands shown in Table 1. The Eight MIXer Receivers (EMIR) and the Fast Fourier Transform Spectrometers (FTS) with a spectral resolution of 200 kHz were used for these observations. The observing procedure was wobbler switching with a throw of $200''$ to ensure flat baselines. In Table 1 we show the Half Power Beam Width (HPBW), spectral resolution and sensitivity achieved in each observed frequency band. The whole dataset will be published elsewhere but this paper is centered on the ionic species and the sulfur compounds.

The unbiased spectral survey has been complemented with $175'' \times 175''$ maps of the SO $2_2 \rightarrow 1_1$, C³⁴S $3 \rightarrow 2$, HCS⁺ $2 \rightarrow 1$, HC¹⁸O⁺ $1 \rightarrow 0$, HOCO⁺ $4_{04} \rightarrow 3_{03}$, DCO⁺ $2 \rightarrow 1$, D¹³CO⁺ $2 \rightarrow 1$, p-H₂CO $2_{02} \rightarrow 2_{01}$, p-H₂¹³CO $2_{02} \rightarrow 2_{01}$ lines (see Fig. 2). These maps were simultaneously observed at 3 and 2 mm with a combination of the EMIR receivers and the Fourier transform spectrometers, which yields a bandwidth of 1.8 GHz per sideband per polarization at a channel spacing of 49 kHz. The tuned frequencies were 85.55 and 144.90 GHz. We used the on-the-fly scanning strategy with a dump time of 0.5 seconds and a scanning speed of $10.9''/\text{s}$ to ensure a sampling of at least 3 dumps per beam at the $17.8''$ resolution of the 2mm lines. The $175'' \times 175''$ region was covered using successive orthogonal scans along the RA and DEC axes. The separation between two successive rasters was $6.5''$ ($\sim \lambda/2D$) to ensure Nyquist sampling at the highest observed frequency, i.e. 145 GHz. A common reference position located at offsets ($200''$, $150''$) was observed for 10 seconds every 77.5 seconds. The typical IRAM-30m position accuracy is $3''$.

The data reduction and the line identification were carried out with the package GILDAS/CLASS software.

3 Methodology

Our goal is to use the database provided by the IRAM Large Program ASAI (PIs: Rafael Bachiller, Bertrand Lefloch) together with previous millimeter data from our group (Marcelino et al., 2005, 2009, 2010; Cernicharo et al., 2012, 2013; Daniel et al., 2013;

See 1. <http://www.iram.fr/IRAMFR/GILDAS> for more information about the GILDAS softwares (Pety, 2005).

Cernicharo et al., 2014; Gerin et al., 2015) and complementary mapping to accurately determine the fundamental chemical parameters.

Within our spectral survey we have detected the following ions: HCO^+ , H^{13}CO^+ , HC^{18}O^+ , HC^{17}O^+ , DCO^+ , D^{13}CO^+ , HOCO^+ , DOCO^+ , HCS^+ , SO^+ , HC^{34}S^+ , DCS^+ , HCNH^+ , H_2COH^+ , HC_3NH^+ , NNH^+ , NND^+ , N^{15}NH^+ and $^{15}\text{NNH}^+$. This is probably the first secure detection of the deuterated ions DCS^+ and DOCO^+ . A tentative detection of DOCO^+ was reported by Fechtenbaum & Bontemps (2013) towards the massive protostar CIGX-N63. Daniel et al. (2013) modeled the emission of NNH^+ , NND^+ , N^{15}NH^+ and $^{15}\text{NNH}^+$ ions in this core. We use their results to compare with our chemical models without repeating the analysis. Our final list of detections is the most complete inventory of molecular ions observed in this source and therefore, an unprecedented opportunity to improve our knowledge of the ionization fraction. The main destruction mechanism of the observed protonated ions is the rapid recombination with e^- to give back the neutral parent species. For this reason, the $[\text{XH}^+]/[\text{X}]$ ratios are very sensitive to the gas ionization fraction and are commonly used to estimate it. In order to compare with chemical models, we also include the lines of the parent molecules in our analysis (see Table. A.1). It is interesting to note that we have not detected CO^+ and HOC^+ . These ions react with molecular hydrogen and only reach significant abundances in the external layers of photon-dominated regions which are not fully molecular (see e.g. Fuente et al., 2003; Rizzo et al., 2003). The non-detection of these ions mainly supports the interpretation that we are probing a dense molecular core in which the ionization is dominated by cosmic rays.

The second key ingredient in gas phase chemical models is the depletion factors. The sensitivity of the chemistry to the elemental abundances in gas phase was discussed by Graedel et al. (1982), who introduced the concept of “low-metal” elemental abundances, in which the abundances of metals, silicon, and sulfur are depleted by a factor of 100 with respect to the values typically used until then (those observed in the diffuse cloud ζ Oph). This choice of elemental abundances provides a reasonable agreement with the observed molecular abundances in dark clouds (see review by Agúndez & Wakelam (2013)). In the last decades there has been increasing evidence that these abundances are decreasing with density because molecules are frozen onto the grain surfaces and reach the lowest values in dense prestellar cores. This phenomenon is quantified by the so called depletion factor, that is the ratio between the total (ice+gas) abundance and the one observed in gas phase. The depletion is defined for a specific molecule or for the total amount of atoms of a given element. The depletion factor of each species depends on the local physical conditions, time evolution and the binding energy. For a given molecule, the depletion factor is evaluated by measuring the gas phase abundance as a function of the gas density within the core. Tafalla et al. (2006) have shown that CO presents a strong variation while the effect is moderate for HCN, and almost null for N_2H^+ .

To determine the depletion factor of a given element is more complex since it depends on the gas chemical composition and eventually, on the binding energy of the compound(s) that are the most abundant. In order to derive the elemental gas abundance of C, O, N and S, we need to include in our analysis the main reservoirs of these elements. The CO abundance is four orders of magnitude larger than that of any other molecule except H_2 . Therefore, we can

assume that in a dense core, such as Barnard 1b, all the carbon is locked in CO. The main reservoirs of nitrogen are atomic nitrogen (N) and molecular nitrogen (N_2) which are not observable. The nitrogen abundance can be derived by applying a chemical model and fitting the observed abundances of nitriles (HCN, HNC, CN) and N_2H^+ . The most abundant oxygenated molecules, O_2 , H_2O and OH, cannot be observed in the millimeter domain and the oxygen depletion factor has to be derived indirectly. In the case of sulfur, the abundance of S-bearing species are very sensitive to the C/O gas-phase ratio, and hence the oxygen depletion factor. A complete chemical modeling is needed to have a reasonable estimate of the O and S depletion factors.

4 Results

Figs. B.1 to B.9 show the spectra of the neutral and protonated species considered in this work. In all cases, the protonated and neutral species present similar line profiles suggesting that both come from the same region. All the lines show two narrow velocity components, at $\sim 6.5 \text{ km s}^{-1}$ and $\sim 7.0 \text{ km s}^{-1}$, respectively. We use the 30m maps to explore the origin of the different species and the two velocity components. The integrated intensity maps of the $SO \ 2_2 \rightarrow 1_1$, $C^{34}S \ 3 \rightarrow 2$, $HCS^+ \ 2 \rightarrow 1$, $HC^{18}O^+ \ 1 \rightarrow 0$, $HOCO^+ \ 4_{04} \rightarrow 3_{03}$, $DCO^+ \ 2 \rightarrow 1$, $D^{13}CO^+ \ 2 \rightarrow 1$, $p\text{-}H_2CO \ 2_{02} \rightarrow 2_{01}$, $p\text{-}H_2^{13}CO \ 2_{02} \rightarrow 2_{01}$ lines are shown in Fig. 2. The emission of the $HC^{18}O^+$, $HOCO^+$, $C^{34}S$, DCO^+ , $D^{13}CO^+$ and SO lines is concentrated in the elongated filament that contains B1b-N and B1b-S (see Fig. 2). The emission of the $N_2H^+ \ 1 \rightarrow 0$ line, as reported by Daniel et al. (2013), is also concentrated in this dense filament. In the case of $HOCO^+$, the elongated emission seems to be slightly shifted to the west although the map is too noisy to conclude. In all these cases, the line intensities are similar towards the N and S protostars. On the contrary, the emission of the $o\text{-}NH_2D \ 1_{11s} \rightarrow 0_{01a}$ line peaks towards B1b-N (Daniel et al., 2013). Another exception is H_2CO whose emission presents an intense peak towards B1b-S. The emission of the $HCS^+ \ 2 \rightarrow 1$ line presents a flat spatial distribution suggesting that is coming from the cloud envelope.

Linewidths can also provide information about the origin of the molecular emission. On basis of low angular resolution observations, Bachiller et al. (1990) proposed a correlation between the linewidths and the depth into the B1 cloud, with the narrowest lines ($\sim 1 \text{ km s}^{-1}$) coming from the highest extinction regions. Similar results were obtained by Daniel et al. (2013) on basis of the observation of HCN, HNC, N_2H^+ , NH_3 , and their isotopologues. The line profiles were well reproduced by a collapsing dense core (infall velocity = 0.1 km s^{-1}) with a turbulent velocity of 0.4 km s^{-1} surrounded by a static lower density envelope with a turbulent velocity of 1.5 km s^{-1} . In Fig. 3, we show the spatial distribution of the linewidths for the set of maps shown in Fig. 2. In agreement with previous works, we find a clear decrease of the linewidth with the distance from the core center in the $SO \ 2_2 \rightarrow 1_1$ line. Linewidths are $\sim 2 \text{ km s}^{-1}$ in the most external layer and decrease to $\sim 0.7 \text{ km s}^{-1}$ towards the core center. However, the linewidths of the $HCS^+ \ 2 \rightarrow 1$ lines are $\sim 2 \text{ km s}^{-1}$ all over the region without a clear pattern. This supports the interpretation of the HCS^+ emission coming from an external layer of the cloud. The only position where the linewidths of the HCS^+ line becomes $< 1 \text{ km s}^{-1}$ is towards the IR star B1b-W. For $HC^{18}O^+$, DCO^+ and $D^{13}CO^+$, we do see a trend, with the linewidths decreasing with the decreasing radius from the core center. However, their linewidths are always $> 1 \text{ km s}^{-1}$ suggesting that the emission is not

dominated by the innermost layers of the envelope. The linewidth of the p-H₂CO line is quite constant over the whole core. This line is more likely optically thick and its emission is only tracing the outer layers of the core.

Fig. 4 and 5 show the spectral maps of the DCO⁺ 2→1 and the SO 2₂→1₁ lines, respectively. The emission of DCO⁺ extends from ~5.5 km s⁻¹ to ~8.0 km s⁻¹, while the SO emission is detected in a narrower velocity range, between ~5.9 km s⁻¹ to ~7.5 km s⁻¹, i.e., SO is mainly coming from the 6.5 km s⁻¹ component. The intensity peak at 6.5 km s⁻¹ is shifted ~5'' west from the peak at 7.0 km s⁻¹. It is interesting to note that DCO⁺ presents an emission peak towards B1b-N at a velocity of ~7.5 km s⁻¹ in agreement with the N₂H⁺ and NH₂D observations by Daniel et al. (2013). Recent interferometric observations revealed the kinematical structure of this region at scales of ~500–1000 AU (Huang & Hirano, 2013; Gerin et al., 2015). Huang & Hirano (2013) detected intense emission of the N₂D⁺ 3→2 lines towards the two protostellar cores B1b-N and B1b-S using the SMA. The N₂D⁺ emission is centered at ~7.0±0.2 km s⁻¹ towards B1b-N, and at ~6.5±0.2 km s⁻¹ towards B1b-S, confirming the existence of the two velocity components.

In the cases of H₂¹³CO, H₂S, HOCO⁺, and in one transition of CCS, OCS and SO₂ (see Table B.1), we detect wings at red-shifted velocities. Compact outflows are detected towards each protostellar core with wings in the 7.5 ± 15 km s⁻¹ velocity range (Gerin et al., 2015). In Fig. 6 we overlay the 30m beam at 3mm and 1mm on the interferometric H₂CO map. The B1b-N outflow and the red wing of the B1b-S outflow lie within our beam at 3mm, but the whole B1b-N outflow and a fraction of the red lobe of the B1b-S outflow are missed in the 2mm and 1mm observations. The emission at the outflow velocities is not taken into account in our calculations because we are only interested in the two velocity components associated with the core emission (see Sect. 5 for details).

5 Column density calculations

In order to investigate abundance variations between the two velocity components, we carried out a separate analysis for each. The spectral resolution of our observations is different for the 3mm, 2mm and 1mm bands. To carry out a uniform analysis, we have degraded the velocity resolution to a common value of 0.25 km s⁻¹, and then fitted Gaussians to each one. In the fitting, we fixed the central velocities to 6.5 km s⁻¹ and ~7.0 km s⁻¹, and the linewidths to $\Delta v=0.7$ km s⁻¹ and 1.0 km s⁻¹, respectively. The fitting returns the integrated intensity for each component. This procedure gives an excellent fit for most lines and neglects possible line wings with velocities >7.5 km s⁻¹. The final integrated intensities are shown in Table B.1. We are aware that this simple method is not able to cleanly separate the contribution from each component. There is some unavoidable velocity overlap between the two components along the line of sight and our spatial resolution is limited (see Fig 4 and Fig 5). However, it can help to detect possible chemical gradients.

Several isotopologues of each molecule have been detected as expected taking into account the large extinction in this core ($A_V \sim 76$ mag). As zero-order approximation, we have derived the column densities and fractional abundances of the different species using the rotation diagram technique. This technique gives a good estimate of the total number of molecules

within our beam as far as the observed lines are optically thin. To be sure of this requirement, we have selected the rarest isotopologue of each species. Furthermore, we assumed that the emission is filling the beam. To calculate the column densities and abundances of the main isotopologues we adopted $^{12}\text{C}/^{13}\text{C}=60$, $^{16}\text{O}/^{18}\text{O}=550$, $^{32}\text{S}/^{34}\text{S}=22.5$ and $^{34}\text{S}/^{33}\text{S}=6$ (Chin et al., 1996; Wilson et al., 1999).

In Table 2 we show the results of our rotational diagram calculations. The errors in the rotation temperatures and column densities are those derived from the least square fitting. There are, however, other kind of uncertainties that are not considered in these numbers. One source of uncertainty is the unknown beam filling factor. Since the beam is dependent on the frequency, this could bias the derived rotation temperature. To estimate the error due to this uncertainty, we have calculated the column densities by an alternative method. Daniel et al. (2013) modeled the density structure of the Barnard 1b core on the basis of dust continuum at 350 μm and 1.2 mm. They obtained that the mean density in the $\sim 29''$ beam is $n(\text{H}_2)\approx 10^5 \text{ cm}^{-3}$. Lis et al. (2010) derived a gas kinetic temperature of, $T_K = 12 \text{ K}$, from NH_3 observations. We adopted these physical conditions to derive the molecular column densities by fitting the integrated intensity of the lowest energy transition using the LVG code MADEX (Cernicharo, 2012). The results are shown in Table 2. Column densities derived using the rotation diagram technique and LVG calculations agree within a factor of 2 for all the compounds. We consider that our estimates are accurate within this factor.

In Table 3 we show the fractional abundances of the studied species and some interesting molecular abundance ratios. To estimate the fractional abundances for each velocity component, we have assumed that the abundance of $^{13}\text{C}^{18}\text{O}$ is the same for the two components and adopted a total molecular hydrogen column density of, $N(\text{H}_2)=7.6 \cdot 10^{22} \text{ cm}^{-2}$ (Daniel et al., 2013). Most of the fractional abundances and abundance ratios agree within the uncertainties for the two velocity components. There are, however, significant chemical differences for some species. One first difference is that the HCO^+ deuterium fraction is a factor ~ 3 higher in the 7 km s^{-1} component than in the 6.5 km s^{-1} one. The spectral velocity maps of the $\text{DCO}^+ 2\rightarrow 1$ and $\text{D}^{13}\text{CO}^+ 2\rightarrow 1$ maps shows that this velocity component is associated with the cold protostar B1b-N. The second difference is that the SO/CS abundance ratio is 2–10 times larger in the $\sim 6.5 \text{ km s}^{-1}$ component than in the $\sim 7.0 \text{ km s}^{-1}$ one. High SO abundances, up to $\sim 10^{-7}$, are found in bipolar outflows because of the release of sulfuretted compounds into the gas phase (Bachiller & Pérez Gutierrez, 1997). One could think that the high SO abundance could then result from the interaction of the cold core with the B1b-S outflow, or, more likely, of the interaction of the dense core with the B1a and/or B1d outflows. However, the profiles of the SO lines are very narrow, the contrary that one would expect if the emission were coming from a shock or a turbulent medium. In Sect. 6, we discuss in detail the sulfur chemistry and possible explanations for this high SO abundance in Barnard 1.

One important result is that the $[\text{XH}^+]/[\text{X}]$ ratios do not present variations between the two velocity components. This supports our interpretation that the ionization fraction is mainly driven by CR and is consistent with the measured H_2 column density ($7.6 \times 10^{22} \text{ cm}^{-2}$). The core is expected to be thorough permeable to CR and the ionization does not present significant fluctuations across the envelope.

6 Chemical modeling

We perform chemical modelling to constrain the physical and chemical properties in Barnard B1b. We do not include here the accretion/desorption mechanisms of gas phase molecules on the grains and rather vary the amount of the elemental abundances of heavy atoms available in the gas phase to mimic these effects. Formation on grains of Hydrogen molecules and its isotopic substituted forms HD and D₂ is however considered explicitly. Such an approach, although primitive, allows to disentangle the main gas phase processes at work. We use both a steady state and time-dependent model to explore the chemistry and verified that the steady state results are recovered by the time-dependent code for sufficiently large evolution time (typically 10 Myr).

Our chemical network contains 261 species linked through more than 5636 chemical reactions. Ortho and para forms of H₂, H₂⁺, H₃⁺, D₂, H₂D⁺, D₂H⁺ and D₃⁺ are explicitly introduced following the pioneering papers of Flower et al. (2004, 2006) for heavily depleted regions and including the chemistry of carbon, oxygen, nitrogen and sulfur. Discriminating between para and ortho forms of H₂ is particularly critical for deuteration in cold regions via the H₃⁺ + HD ↔ H₂D⁺ + H₂ reaction as the endothermicity of the reverse reaction is of the same order of magnitude than the rotational energy of H₂, as first emphasized by Pagani et al. (1992). Nitrogen chemistry is also very sensitive to the ortho/para forms of H₂ as pointed out by Le Boulrot (1991) due to the small endoergicity of the N⁺ + H₂ → NH⁺ + H reaction. Whereas a definitive understanding of this reaction is still pending (Zymak et al., 2013), we follow the prescription of Dislaire et al. (2012) for the reaction rate coefficients of N⁺ + H₂(p/o) reaction. Our chemical network also contains the recent updates coming from experimental studies of reactions involving neutral nitrogen atoms as reviewed in Wakelam et al. (2013). We also introduced species containing two nitrogen atoms such as C₂N₂, C₂N₂H⁺ following the recent detection of C₂N₂H⁺ by Agúndez et al. (2015) for which the reaction rate coefficients have essentially been taken from the UMIST astrochemical database (McElroy et al., 2013). An important and non fully recognized feature is the link between sulfur and nitrogen chemistry as shown by the detection of NS, which is found both in regions of massive star formation and in cold dark clouds (McGonagle et al., 1994; McGonagle & Irvine, 1997). The main formation reaction is through S + NH whose rate is given as 10⁻¹⁰ cm³ s⁻¹ in astrochemical databases, which then also induces that sulfur chemistry may depend on o/p ratio of H₂.

Our methodology is the following: we run the time-dependent model for a set of standard elemental abundances and cosmic ray ionization rate to determine which molecular abundances and molecular abundance ratios reach the steady state in a few 0.1–1 Myr, the estimated age for Barnard B1b. These molecular abundances and abundance ratios are expected to be in equilibrium and are used to explore the parameter space using steady-state calculations. On basis of the steady-state calculations, we select the most plausible values and run the time-dependent model to confirm that our fit is correct. In all our calculations, we assume uniform physical conditions and fix n(H₂)=10⁵ cm⁻³ and T_k=12 K, according with previous works (Lis et al., 2010; Daniel et al., 2013). We iterate several times to get the

best match with the observations. The predictions of our best fit model are compared with observations in Fig. 7 and 8.

6.1 Cosmic ray ionization rate

The $[\text{HCO}^+]/[\text{CO}]$ ratio has been extensively used to estimate the cosmic ray ionization rate. The results of our time dependent model confirms that it is, very likely, the most reliable diagnostic since it reaches the equilibrium in 0.1 Myr and its chemistry is well known. Other $[\text{XH}^+]/[\text{X}]$ ratios, such as $[\text{HCS}^+]/[\text{CS}]$ and $[\text{HCNH}^+]/[\text{HCN}]$, are also expected to be in equilibrium at the typical ages of a molecular cloud. Fig. 9 shows the variation of the $[\text{HCO}^+]/[\text{CO}]$, $[\text{HCNH}^+]/[\text{HCN}]$ and $[\text{HCS}^+]/[\text{CS}]$ as a function of the cosmic ray ionization rate in steady-state calculations. Assuming an uncertainty of a factor of 2 in the derived abundance ratios, values of ζ_{H_2} in the interval between $3 \times 10^{-17} \text{ s}^{-1}$ to $1 \times 10^{-16} \text{ s}^{-1}$ are consistent with the observed $[\text{HCO}^+]/[\text{CO}]$ and $[\text{HCNH}^+]/[\text{HCN}]$ ratios. These values are in the upper end of the values inferred for cloud cores (Caselli et al., 1998), and are higher than those of the typical dark cloud L1544, $\zeta_{\text{H}_2} \sim 1 \times 10^{-18}$ (Galli & Padovani, 2015). This could explain the higher gas and dust temperature in this dense core, $T_d \sim 12 \text{ K}$, compared with dust temperature in L1544, $T_d < 6-8 \text{ K}$ (Crapsi et al., 2007).

The $[\text{HCS}^+]/[\text{CS}]$ ratio is not fitted by any reasonable value of ζ_{H_2} . This is not surprising since the HCS^+ emission is mainly coming from the low density envelope. In Fig. 7 we show model predictions for a density of $n(\text{H}_2) = 10^4 \text{ cm}^{-3}$. The abundances of most molecules decrease while the HCS^+ abundance remains constant and that of CCS increases. We would like to note that these calculations have been done assuming the same elemental abundances as in the high density case. This is not realistic since lower depletions are expected in the envelope and therefore, the HCS^+ abundance would be higher. Moreover, this core is illuminated on its eastern side by the nearby Herbig Ae stars LkHa 327 and LkHa 328 (Walawender et al., 2009; Young et al., 2015). The UV photons are expected to increase the HCS^+ abundance. In fact, the $\text{HCS}^+ 2 \rightarrow 1$ emission is maximum towards the illuminated side (see Fig. 1).

Our estimate of the cosmic ray ionization rate, permits us to have an estimate of the N_2 abundance in this core. Being one of the main nitrogen reservoirs, N_2 cannot be observed at (sub-)millimeter wavelengths because of its lack of dipole moment. We can only estimate its abundance indirectly through the protonated compound, N_2H^+ . The N_2H^+ abundance is very sensitive to the cosmic ray ionization rate. In Fig. 9, we present the $[\text{N}_2\text{H}^+]/[\text{N}_2]$ ratio as a function of the cosmic ray ionization rate. Assuming $\zeta_{\text{H}_2} = 4 \times 10^{-17} \text{ s}^{-1}$ and on basis of our observational data, we derive $[\text{N}_2] \sim 8 \times 10^{-5}$ which is consistent with the typical value of the N elemental abundance in a dark cloud, $\text{N}/\text{H} = 6.4 \times 10^{-5}$.

The HOCO^+ molecule (protonated carbon dioxide) is thought to form via a standard ion-molecule reaction, the transfer of a proton from H_3^+ to CO_2 (see e.g. Turner et al., 1999). To date HOCO^+ has been detected towards the Galactic center, a few starless translucent clouds (Turner et al., 1999), a single low-mass Class 0 protostar (Sakai et al., 2008) and the protostellar shock L1157-B1 (Podio et al., 2014). Interestingly, this molecule is particularly abundant, $\sim 10^{-9}$, in the Galactic Center region (Minh et al., 1988, 1991; Deguchi et al.,

2006; Neill et al., 2014). We derive an HOCO^+ abundance of $\sim 10^{-11}$, i.e. two orders of magnitude lower than that derived in the Galactic center clouds (Deguchi et al., 2006; Neill et al., 2014) and L1157-B1 (Podio et al., 2014), and a factor of ~ 10 lower than that in translucent clouds (Turner et al., 1999). This is not unexpected since the HOCO^+ abundance is inversely proportional to the gas density (Sakai et al., 2008) and B1b is a dense core. Our model underpredicts by a factor 200 the HOCO^+ abundance (see Fig. 7). As commented below, HOCO^+ is proxy of CO_2 and the latter is not efficiently formed in gas phase (Turner et al., 1999).

The lack of an electric dipole moment of CO_2 makes gas phase detections difficult. The abundance of CO_2 in the solid phase has been investigated through its two vibrational modes at 4.3 and 15.0 μm . In the solid phase, the typical abundance is $\sim 10^{-6}$ relative to total H_2 (Gerakines et al., 1999; Gibb et al., 2004). In the gas phase, the typical detected abundance is $1\text{--}3 \times 10^{-7}$ (van Dishoeck et al., 1996; Boonman et al., 2003; Sonnentrucker et al., 2006). Assuming the $[\text{HOCO}^+]/[\text{CO}_2]$ ratio predicted by our model, 2.2×10^{-4} , we estimate a CO_2 abundance of $\sim 5 \times 10^{-8}$. This value is in the lower end of that measured in star forming regions but 200 times larger than that predicted by our gas-phase model. Photodesorption and sputtering of the icy mantles are more likely the main CO_2 production mechanism.

6.2 Sulfur chemistry: C, O and S elemental abundances

The initial elemental abundances in gas phase are an essential parameter in the chemical modeling. In cloud cores ($A_V > 10$ mag), as long as the C elemental abundance is lower than O, we can assume that the abundance of C is equal to that of CO and conclude that $C/H = 1.7 \times 10^{-5}$. (Note that fractional abundances are given with respect to H_2 .) The main source of uncertainty in this value comes from the uncertainty in the CO abundance which is estimated to be a factor of 2.

To estimate the amount of S in gas phase requires a detailed modeling of its chemistry. As shown in Fig. 10, the cosmic ray ionization rate is a critical parameter to estimate the S/H. The main sulfur reservoirs in a dense core are atomic sulfur (S) and SO (see Fig. 12). Unfortunately, chemical models make a poor work in predicting the fractional abundance of SO since it dramatically depends on two factors: i) the $\text{S} + \text{O}_2 \rightarrow \text{SO} + \text{O}$ and $\text{S} + \text{OH} \rightarrow \text{SO} + \text{H}$ reaction rates and ii) the O_2 and OH abundances.

The $\text{S} + \text{O}_2$ reaction rate coefficient at low temperatures is not known. Experimental measurements have only been performed above 200 K. Lu et al. (2004) have reviewed the various theoretical and experimental results and adopted a value of $2 \times 10^{-12} \text{ cm}^3 \text{ s}^{-1}$ at 298 K. The UMIST and KIDA databases suggest different values. In KIDA, a constant value of $2.1 \times 10^{-12} \text{ cm}^3 \text{ s}^{-1}$ is suggested in the 250–430 K temperature range whereas the latest version of the UMIST database give $1.76 \times 10^{-12} (T/300)^{0.81} \exp(30.8/T) \text{ cm}^3 \text{ s}^{-1}$ in the 200–3460 K temperature interval. This small activation barrier would imply rates as low as $10^{-23} \text{ cm}^3 \text{ s}^{-1}$ at the temperature of 12 K and a decrease in the SO, SO_2 and SO^+ abundances. Quasiclassical trajectory calculations were carried out for the reaction $\text{S} + \text{O}_2$ and its reverse by Rodrigues & Varandas (2003). With 6000 trajectories they obtain that the reaction rate remains constant or decrease very slowly for temperatures between 50 K and 1000 K. Using the same potential, we have performed new quasiclassical trajectory

calculations with 100000 trajectories for temperatures between 10 K and 50 K (see Appendix A). Our results confirm that the reaction rate remains quite constant (within 30%) in the 10 K to 50 K range. Therefore, we adopted the KIDA value, $2.1 \times 10^{-12} \text{ cm}^3 \text{ s}^{-1}$, in our calculations.

The second more important reaction for the formation of SO is $\text{S} + \text{OH}$. DeMore et al. (1997) measured a value of $6.6 \times 10^{-11} \text{ cm}^3 \text{ s}^{-1}$ at 398 K that is the one adopted in our calculations. Recent theoretical calculations by Goswami et al. (2014) predicted a value a factor of ~ 2 lower. These calculations were performed for a range of temperatures between 10–500 K and the reaction rate remains quite constant over this range with an increase of a factor of ~ 1.6 for temperatures close to 10 K. We adopted the experimental value is very likely good in a factor of 2 for the physical conditions of B1.

The oxygen and sulfur chemistries are tightly linked. Since S is rapidly converted to SO by reacting with O_2 and OH, its abundance is very dependent on the amount of molecular oxygen in gas phase, that itself depends on the C/O ratio (see Fig 10). Conversely, a large abundance of S in gas phase ($>10^{-6}$) leads to a rapid destruction of O_2 and decreases the $[\text{O}_2]/[\text{O}]$ ratio (see Fig 11). We find a good agreement with the observations assuming C/O=0.6 and S/H in the interval between 6×10^{-7} and 10^{-6} . With these parameters we have an excellent fit of the SO abundance and the $[\text{SO}]/[\text{CS}]$, $[\text{SO}_2]/[\text{SO}]$ and $[\text{H}_2\text{CS}]/[\text{CS}]$ ratios although the agreement is worse for OCS (Fig 9 and 10). We do not have any good explanation for the low observed abundance of OCS. It may be frozen onto the grain mantles in this cold core. But taking into account the limitations of our model, one single $n(\text{H}_2)$ and T, we consider that the agreement is quite good. Assuming these values, our chemical model predicts a steady state O_2 abundance of $\sim 4 \times 10^{-7}$. There is no measurement of the O_2 abundance in B1b, but this predicted abundance is higher than the upper limits derived for other dark clouds (Pagani et al., 2003), and that reported in ρ Oph A ($\sim 5 \times 10^{-8}$) (Liseau et al., 2012)). The low O_2 abundance measured in dark clouds is usually explained in terms of time evolution. O_2 is a late-type molecule that presents low abundance ($\sim 10^{-8}$) at typical ages of dark clouds (a few 0.1 Myr). Another possibility is that O_2 becomes frozen on grain mantles. Regarding the sulfur chemistry, we would like to comment that a lower O_2 abundance would decrease the SO production via the $\text{S} + \text{O}_2$. In this case, we would need to increase S/H to reproduce the observations and our estimate would be a lower limit.

Finally, our chemical model does not include surface chemistry. The main effect of dust grains is to decrease the abundance of sulfur bearing molecules, especially SO_2 , because of adsorption on grain mantles. The most abundant species in Barnard 1b, SO, is thought to form in gas phase. As long as it remains true, we consider that our measurement of the sulfur depletion is reliable.

7 Barnard B1b chemistry

We have used a state-of-the-art gas phase model to derive the cosmic ionization rate and the elemental abundances towards the dense core Barnard 1b. Our model fit predicts the observed abundances and abundance ratios reasonably well (within a factor of two), but it fails, by several orders of magnitude to predict the abundances of HCS^+ and HOCO^+ (see

Fig. 6 and 7). As commented above, HCS^+ is very likely coming from the lower density envelope instead of the dense core and cannot be accounted by our single point (n,T) model. In the case of HOCO^+ , the model failure is not surprising since CO_2 is mainly formed by surface reactions.

In Table 4 we compare the initial abundances derived towards Barnard 1b with typical values in dark clouds and diffuse clouds (Agúndez & Wakelam, 2013). The depletion of C and O is 10 times larger than those measured in prototypical dark clouds such as TMC 1 and L134N. These values are similar to those found in pre-stellar cores and young stellar objects where high values of CO depletion (~ 5 – 10) and high deuterium fractions (~ 0.01) are measured (Caselli et al., 1999; Jørgensen et al., 2002; Crapsi et al., 2005; Emprechtinger et al., 2009; Alonso-Albi et al., 2010). High deuterium fractions are observed in Barnard 1b (Lis et al., 2002; Marcelino et al., 2005) which further confirm this similarity. However, the relatively low S depletion in this source is unexpected. A sulfur depletion factor of ~ 100 is adopted to explain the chemistry in dark clouds and dense cores (Tafalla et al., 2006; Agúndez & Wakelam, 2013). A higher gas phase sulfur abundance approaching the solar value of 1.5×10^{-5} , has only been found in bipolar outflows (Bachiller & Pérez Gutiérrez, 1997; Anderson et al., 2013), photodissociation regions (Goicoechea et al., 2006) and hot cores (Esplugues et al., 2013, 2014). In these cases, it has been interpreted as the consequence of the release of the S-species from the icy grain mantles because of thermal and non-thermal desorption and sputtering. Contrary to dark clouds and pre-stellar cores, in Barnard 1b the S depletion is comparable to that of C and O, which explains the high abundances of S-bearing species in this core.

The abundance of sulfur in grains is very uncertain. Thus far, the only S-bearing molecule unambiguously detected in ice mantles is OCS, because of its large band strength in the infrared (Geballe et al., 1985; Palumbo et al., 1995), and maybe SO_2 (Boogert et al., 1997), but there are only upper limits of the solid H_2S abundance (Jiménez-Escobar & Muñoz Caro, 2011) which is thought to be the main sulfur reservoir in the ice. Measurements of the sulfur depletion are derived by comparing the predictions of gas phase chemical models with the observed abundances of the main S-bearing species. As reported above, chemical models are limited by the uncertainty in the reaction rates and the poorly known $[\text{O}]/[\text{O}_2]$ ratio and the exact value of the sulfur depletion is uncertain. But our results suggests that the sulfur depletion in Barnard 1b is not as extreme as in dark clouds where the abundance of S-bearing species is lower.

This moderate sulfur depletion could be the consequence of the star formation activity in the region. B1b is irradiated on its eastern side by UV photons from the nearby Herbig Ae stars LkH α 327 and LkH α 328 (Walawender et al., 2009; Young et al., 2015). On its western side, it is impacted by the outflows associated with B1a and B1d (Hatchell et al., 2007). Not unrelated, the level of turbulence in B1 ($\sim 0.4 \text{ km s}^{-1}$) is higher than in cold cores like L1544, TMC-1 or L134N ($\sim 0.1 \text{ km s}^{-1}$). Sputtering induced by collisions may be efficient in this turbulent environment to erode the icy mantles and release the sulfuretted species to the gas phase. Sputtering could also explain the high abundances of complex molecules observed in this core (Marcelino et al., 2009; Cernicharo et al., 2012). The main drawback of this interpretation is that it would also imply a low depletion of CO that is not observed.

Another possibility is that the moderate sulfur depletion is a consequence of the rapid collapse of B1b. Aikawa et al. (2005) have investigated the impact of different collapse timescales on the gas chemistry. The initial conditions of their first model lie close to the critical Bonnor-Ebert sphere with a central density of $\sim 10^4 \text{ cm}^{-3}$. When the central density of the core reaches 10^5 cm^{-3} , the S-bearing species were totally depleted at $R \sim 5000 \text{ AU}$. In the second case, internal gravity overwhelms pressure and the collapse is much faster (about 0.1 Myr). When the central density of the core reaches 10^5 cm^{-3} , molecules such as CS, SO and C_2S have abundances $\sim 10^{-10}$ in the core center while CO is significantly depleted. These abundances are too low compared with our measurements, but it is partially due to the adopted S elemental abundance in the Aikawa's model ($\text{S}/\text{H} = 9.14 \times 10^{-8}$). We would like to remind that we have not targeted the position of the protostar but a nearby position at $R \sim 2500 \text{ AU}$. Finally, our position is spatially coincident with the red wing of the B1b-S outflow. Higher spatial resolution observations are needed to determine the possible influence of the the B1b-S outflow on the S chemistry.

Summarizing, we propose that the low sulfur depletion in this region could be the result of two different factors, both related with the star formation activity. The enhanced UV fields and the surrounding outflows could be the cause of a peculiar initial conditions with low sulfur depletion and high abundances of complex molecules. The star formation activity could also have induced a rapid collapse of the B1-b core that preserves the high abundances of the sulfuretted species. The compact outflow associated with B1b-S could also heat the surroundings and contribute to halt the depletion of S-molecules.

8 Summary and conclusions

- On the basis of our spectral survey towards Barnard 1b, we have selected a set of neutral and ionic species to determine the value of the cosmic ray ionization rate and depletion factors of the C, N, O and S. These are the parameters that determine the gas ionization fraction and hence, the dynamical evolution of this core.
- We have detected the following ions: HCO^+ , H^{13}CO^+ , HC^{18}O^+ , HC^{17}O^+ , DCO^+ , D^{13}CO^+ , HOCO^+ , DOCO^+ , HCS^+ , SO^+ , HC^{34}S^+ , DCS^+ , HCNH^+ , H_2COH^+ , HC_3NH^+ , NNH^+ , NND^+ , N^{15}NH^+ and $^{15}\text{NNH}^+$. This is the most complete inventory of molecular ions in this core and, probably, the first secure detection of the deuterated ion DOCO^+ and DCS^+ in any source. The observational data are well fitted with ζ_{H_2} between $3 \times 10^{-17} \text{ s}^{-1}$ and 10^{-16} s^{-1} . On basis of the HOCO^+ and N_2H^+ observations, we derive abundances of $\sim 4 \times 10^{-8}$ and $(6.4-8) \times 10^{-5}$ for CO_2 and N_2 , respectively.
- We use a state-of-art pseudo-time-dependent gas-phase chemical model that includes the ortho and para forms of H_2 , H_2^+ , D_2^+ , H_3^+ , H_2D^+ , D_2H^+ , D_2 and D_3^+ . Our model assumes $n(\text{H}_2) = 10^5 \text{ cm}^{-3}$ and $T_k = 12 \text{ K}$, derived from previous works. The observational data are well fitted with $\zeta_{\text{H}_2} = (3-10) \times 10^{-17} \text{ s}^{-1}$ and the following elemental abundances: $\text{O}/\text{H} = 3 \times 10^{-5}$, $\text{N}/\text{H} = (6.4-8) \times 10^{-5}$, $\text{C}/\text{H} = 1.7 \times 10^{-5}$ and $\text{S}/\text{H} = (6.0-10) \times 10^{-7}$.

- Barnard 1b presents similar depletion of C and O than those measured in pre-stellar cores. However, the depletion of S is moderate, more similar to that found in bipolar outflows, hot cores and photon-dominated regions. This high C and O depletion, together with the moderate S depletion, produces a peculiar chemistry very rich in sulfuretted species.
- We propose that the low S depletion is the consequence of the peculiar initial conditions (important outflows and enhanced UV fields in the surroundings) and a rapid collapse (~ 0.1 Myr) that permits to maintain most S- and N-bearing species in gas phase. The compact outflow associated with B1b-S could also contribute to enhance the abundance of S-molecules.

Appendix

Refer to Web version on PubMed Central for supplementary material.

Acknowledgements

We thank the Spanish MINECO for funding support from grants CSD2009-00038, FIS2012-32096, FIS2014-52172-C2 AYA2012-32032, and ERC under ERC-2013-SyG, G. A. 610256 NANOCOSMOS. We thank Prof. J.A.C. Varandas for sending us the fortran code of their potential energy surface for the S+O₂ reaction. ER and MG thanks the INSU/CNRS programme PCMI for funding. This research used the facilities of the Canadian Astronomy Data Centre operated by the National Research Council of Canada with the support of the Canadian Space Agency.

References

- Agúndez M, Cernicharo J, de Vicente P, et al. *A&A*. 2015; 579:L10.
- Agúndez M, Wakelam V. *Chemical Reviews*. 2013; 113:8710. [PubMed: 24099569]
- Aikawa Y, Herbst E, Roberts H, Caselli P. *ApJ*. 2005; 620:330.
- Alonso-Albi T, Fuente A, Crimier N, et al. *A&A*. 2010; 518:A52.
- Anderson DE, Bergin EA, Maret S, Wakelam V. *ApJ*. 2013; 779:141.
- Bachiller R, Cernicharo J. *A&A*. 1984; 140:414.
- Bachiller R, Menten KM, del Rio Alvarez S. *A&A*. 1990; 236:461.
- Bachiller R, Pérez Gutiérrez M. *ApJ*. 1997; 487:L93.
- Bergin EA, Plume R, Williams JP, Myers PC. *ApJ*. 1999; 512:724.
- Boogert ACA, Schutte WA, Helmich FP, Tielens AGGM, Wooden DH. *A&A*. 1997; 317:929.
- Boonman AMS, Doty SD, van Dishoeck EF, et al. *A&A*. 2003; 406:937.
- Caselli P, Benson PJ, Myers PC, Tafalla M. *ApJ*. 2002; 572:238.
- Caselli P, Walmsley CM, Tafalla M, Dore L, Myers PC. *ApJ*. 1999; 523:L165.
- Caselli P, Walmsley CM, Terzieva R, Herbst E. *ApJ*. 1998; 499:234.
- Cernicharo, J. *EAS Publications Series*. *EAS Publications Series*. Stehlé, C.; Joblin, C.; d'Hendecourt, L., editors. Vol. 58. 2012. p. 251-261.
- Cernicharo J, Bailleux S, Alekseev E, et al. *ApJ*. 2014; 795:40.
- Cernicharo J, Marcelino N, Roueff E, et al. *ApJ*. 2012; 759:L43.
- Cernicharo J, Tercero B, Fuente A, et al. *ApJ*. 2013; 771:L10.
- Chin Y-N, Henkel C, Whiteoak JB, Langer N, Churchwell EB. *A&A*. 1996; 305:960.
- Crapsi A, Caselli P, Walmsley CM, et al. *ApJ*. 2005; 619:379.
- Crapsi A, Caselli P, Walmsley MC, Tafalla M. *A&A*. 2007; 470:221.
- Dalgarno A, Lepp S. *ApJ*. 1984; 287:L47.
- Daniel F, Gérin M, Roueff E, et al. *A&A*. 2013; 560:A3.

- Deguchi S, Miyazaki A, Minh YC. PASJ. 2006; 58:979.
- DeMore WB, Sander SP, Golden DM, Hampson RF, Kurylo MJ, et al. JPL Publication. 1997; 97(4):1.
- Dislaire V, Hily-Blant P, Faure A, et al. A&A. 2012; 537:A20.
- Dorta-Urra A, Zanchet A, Roncero O, Aguado A. J Chem Phys. 2015; 142:154301. [PubMed: 25903884]
- Emprechtinger M, Caselli P, Volgenau NH, Stutzki J, Wiedner MC. A&A. 2009; 493:89.
- Esplugues GB, Tercero B, Cernicharo J, et al. A&A. 2013; 556:A143.
- Esplugues GB, Viti S, Goicoechea JR, Cernicharo J. A&A. 2014; 567:A95.
- Fechtenbaum, S.; Bontemps, S. SF2A-2013: Proceedings of the Annual meeting of the French Society of Astronomy and Astrophysics. Cambresy, L.; Martins, F.; Nuss, E.; Palacios, A., editors. 2013. p. 219-222.
- Flower DR, Pineau des Forêts G, Walmsley CM. A&A. 2004; 427:887.
- Flower DR, Pineau Des Forêts G, Walmsley CM. A&A. 2006; 449:621.
- Fuente A, Rodríguez-Franco A, García-Burillo S, Martín-Pintado J, Black JH. A&A. 2003; 406:899.
- Galli D, Padovani M. ArXiv. 2015 e-prints.
- Geballe TR, Baas F, Greenberg JM, Schutte W. A&A. 1985; 146:L6.
- Gerakines PA, Whittet DCB, Ehrenfreund P, et al. ApJ. 1999; 522:357.
- Gerin M, Pety J, Fuente A, et al. A&A. 2015; 577:L2.
- Gibb EL, Whittet DCB, Boogert ACA, Tielens AGGM. ApJS. 2004; 151:35.
- Glassgold AE, Galli D, Padovani M. ApJ. 2012; 756:157.
- Glassgold AE, Langer WD. ApJ. 1973; 179:L147.
- Goicoechea JR, Pety J, Gerin M, et al. A&A. 2006; 456:565.
- Goswami S, Rajagopala Rao T, Mahapatra S, Bussery-Honvault B, Honvault P. J Phys Chem A. 2014; 118:5915. [PubMed: 25010948]
- Graedel TE, Langer WD, Frerking MA. ApJS. 1982; 48:321.
- Guelin M, Langer WD, Snell RL, Wootten HA. ApJ. 1977; 217:L165.
- Hatchell J, Fuller GA, Richer JS. A&A. 2007; 472:187.
- Hatchell J, Richer JS, Fuller GA, et al. A&A. 2005; 440:151.
- Hiramatsu M, Hirano N, Takakuwa S. ApJ. 2010; 712:778.
- Hirano, N.; Kamazaki, T.; Mikami, H.; Ohashi, N.; Umemoto, T. Star Formation 1999. Nakamoto, T., editor. 1999. p. 181-182.
- Huang Y-H, Hirano N. ApJ. 2013; 766:131.
- Jiménez-Escobar A, Muñoz Caro GM. A&A. 2011; 536:A91.
- Jørgensen JK, Harvey PM, Evans NJ II, et al. ApJ. 2006; 645:1246.
- Jørgensen JK, Schöier FL, van Dishoeck EF. A&A. 2002; 389:908.
- Karplus M, Porter RN, Sharma RD. J Chem Phys. 1965; 43:3259.
- Le Boulrot J. A&A. 1991; 242:235.
- Lis DC, Roueff E, Gerin M, et al. ApJ. 2002; 571:L55.
- Lis DC, Wootten A, Gerin M, Roueff E. ApJ. 2010; 710:L49.
- Liseau R, Goldsmith PF, Larsson B, et al. A&A. 2012; 541:A73.
- Lu C-W, Wu Y-J, Lee Y-P, Zhu RS, Lin MC. J Chem Phys. 2004; 121:8271. [PubMed: 15511147]
- Marcelino N, Brünken S, Cernicharo J, et al. A&A. 2010; 516:A105.
- Marcelino N, Cernicharo J, Roueff E, Gerin M, Mauersberger R. ApJ. 2005; 620:308.
- Marcelino N, Cernicharo J, Tercero B, Roueff E. ApJ. 2009; 690:L27.
- McElroy D, Walsh C, Markwick AJ, et al. A&A. 2013; 550:A36.
- McGonagle D, Irvine WM. ApJ. 1997; 477:711.
- McGonagle D, Irvine WM, Ohishi M. ApJ. 1994; 422:621.
- McKee CF. ApJ. 1989; 345:782.
- Minh YC, Brewer MK, Irvine WM, Friberg P, Johansson LEB. A&A. 1991; 244:470.

- Minh YC, Irvine WM, Ziurys LM. *ApJ*. 1988; 334:175.
- Neill JL, Bergin EA, Lis DC, et al. *ApJ*. 2014; 789:8.
- Öberg KI, Bottinelli S, Jørgensen JK, van Dishoeck EF. *ApJ*. 2010; 716:825.
- Padovani M, Hennebelle P, Galli D. *A&A*. 2013; 560:A114.
- Pagani L, Olofsson AOH, Bergman P, et al. *A&A*. 2003; 402:L77.
- Pagani L, Salez M, Wannier PG. *A&A*. 1992; 258:479.
- Palumbo ME, Tielens AGGM, Tokunaga AT. *ApJ*. 1995; 449:674.
- Pety, J. SF2A-2005: Semaine de l'AstroPhysique Francaise. Casoli, F.; Contini, T.; Hameury, JM.; Pagani, L., editors. 2005. p. 721
- Pezzuto S, Elia D, Schisano E, et al. *A&A*. 2012; 547:A54.
- Podio L, Lefloch B, Ceccarelli C, Codella C, Bachiller R. *A&A*. 2014; 565:A64.
- Rizzo JR, Fuente A, Rodríguez-Franco A, García-Burillo S. *ApJ*. 2003; 597:L153.
- Rodrigues SPJ, Sabín JA, Varandas AJC. *J Phys Chem A*. 2002; 106:556.
- Rodrigues SPJ, Varandas AJC. *J Phys Chem A*. 2003; 107:5369.
- Sakai N, Sakai T, Aikawa Y, Yamamoto S. *ApJ*. 2008; 675:L89.
- Sonnentrucker P, González-Alfonso E, Neufeld DA, et al. *ApJ*. 2006; 650:L71.
- Tafalla M, Santiago-García J, Myers PC, et al. *A&A*. 2006; 455:577.
- Turner BE, Terzieva R, Herbst E. *ApJ*. 1999; 518:699.
- van Dishoeck EF, Helmich FP, de Graauw T, et al. *A&A*. 1996; 315:L349.
- Wakelam V, Herbst E, Le Bourlot J, et al. *A&A*. 2010; 517:A21.
- Wakelam V, Smith IWM, Loison J-C, et al. *ArXiv*. 2013 e-prints.
- Walawender J, Reipurth B, Bally J. *AJ*. 2009; 137:3254.
- Wilson TL, Mauersberger R, Gensheimer PD, Muders D, Bieging JH. *ApJ*. 1999; 525:343.
- Wootten A, Snell R, Glassgold AE. *ApJ*. 1979; 234:876.
- Young KE, Young CH, Lai S-P, Dunham MM, Evans NJ II. *AJ*. 2015; 150:40.
- Zymak I, Hejduk M, Mulin D, et al. *ApJ*. 2013; 768:86.

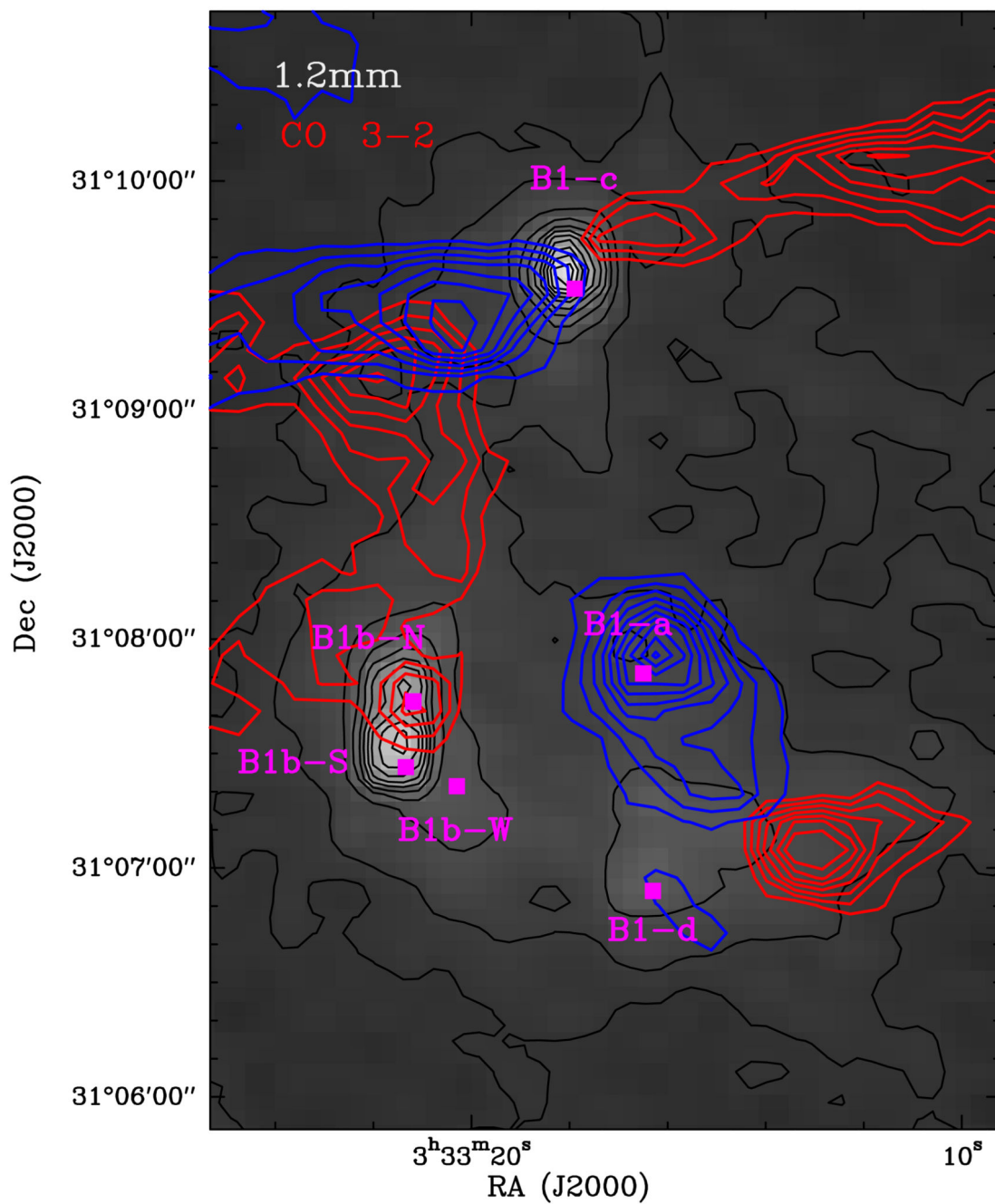


Fig. 1. Continuum map at 1.2 mm observed at the IRAM telescope with the MAMBO instrument (Daniel et al., 2013). The contours are 20 mJy/beam, 40 mJy/beam to 400 mJy/beam steps of by 40 mJy/beam. Contours show the high velocity blue (2.5 to 4.5 km s⁻¹) and red (8.5 to 11.5 km s⁻¹) emission of the CO 3→2 line as observed with the JCMT (project S12AC01).

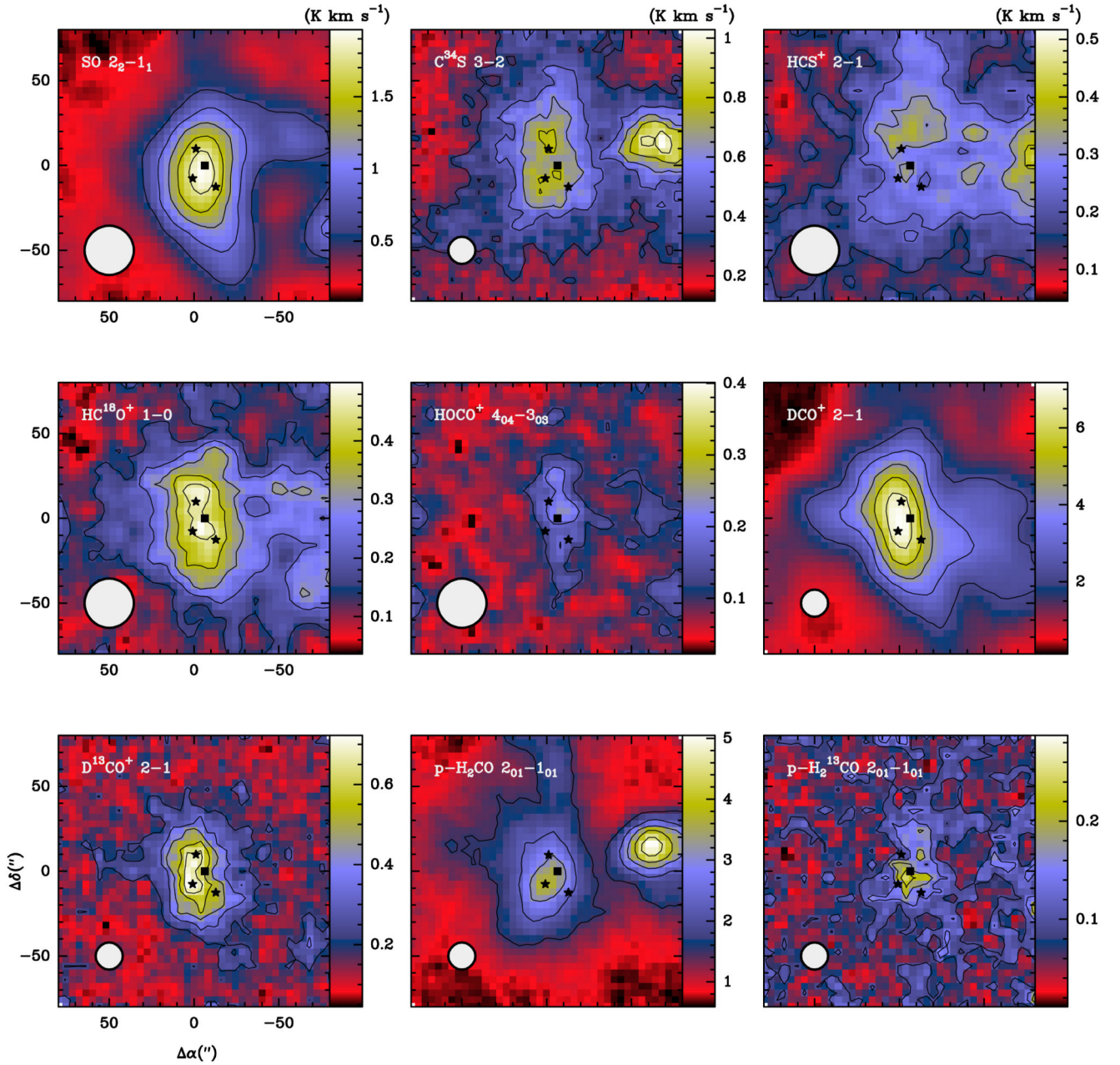


Fig. 2.

Integrated intensity maps of the $\text{SO } 2_2 \rightarrow 1_1$, $\text{C}^{34}\text{S } 3 \rightarrow 2$, $\text{HCS}^+ 2 \rightarrow 1$, $\text{HC}^{18}\text{O}^+ 1 \rightarrow 0$, $\text{HOCO}^+ 4_{04} \rightarrow 3_{03}$, $\text{DCO}^+ 2 \rightarrow 1$, $\text{D}^{13}\text{CO}^+ 2 \rightarrow 1$, $\text{p-H}_2\text{CO } 2_{02} \rightarrow 2_{01}$ and $\text{p-H}_2^{13}\text{CO } 2_{02} \rightarrow 2_{01}$ lines. The HPBW of the 30m telescope at each line frequency is drawn in the bottom-left corner of the panel. The stars indicate the positions of B1b-N and B1b-S and B1b-W. The black square shows the position targeted in the unbiased spectral survey and the beams of the 30m telescope at 3mm ($29''$) and 1mm ($11''$) are drawn towards it.

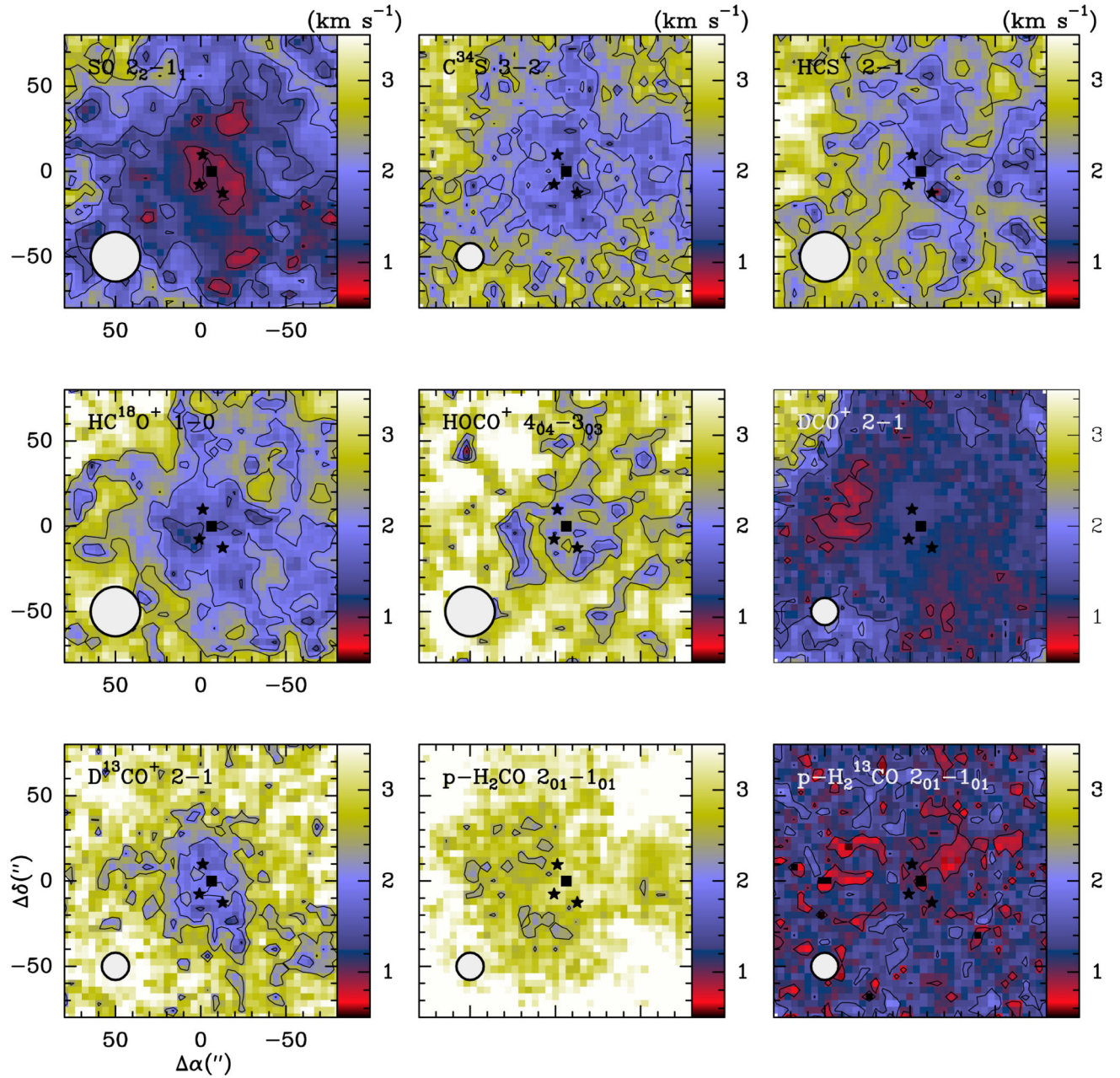


Fig. 3. Maps of the linewidths of the $\text{SO } 2_2 \rightarrow 1_1$, $\text{C}^{34}\text{S } 3 \rightarrow 2$, $\text{HCS}^+ 2 \rightarrow 1$, $\text{HC}^{18}\text{O}^+ 1 \rightarrow 0$, $\text{HOCO}^+ 4_{04} \rightarrow 3_{03}$, $\text{DCO}^+ 2 \rightarrow 1$, $\text{D}^{13}\text{CO}^+ 2 \rightarrow 1$, $\text{p-H}_2\text{CO } 2_{02} \rightarrow 1_{01}$, $\text{p-H}_2^{13}\text{CO } 2_{02} \rightarrow 1_{01}$ lines. Symbols are the same as in Fig. 2.

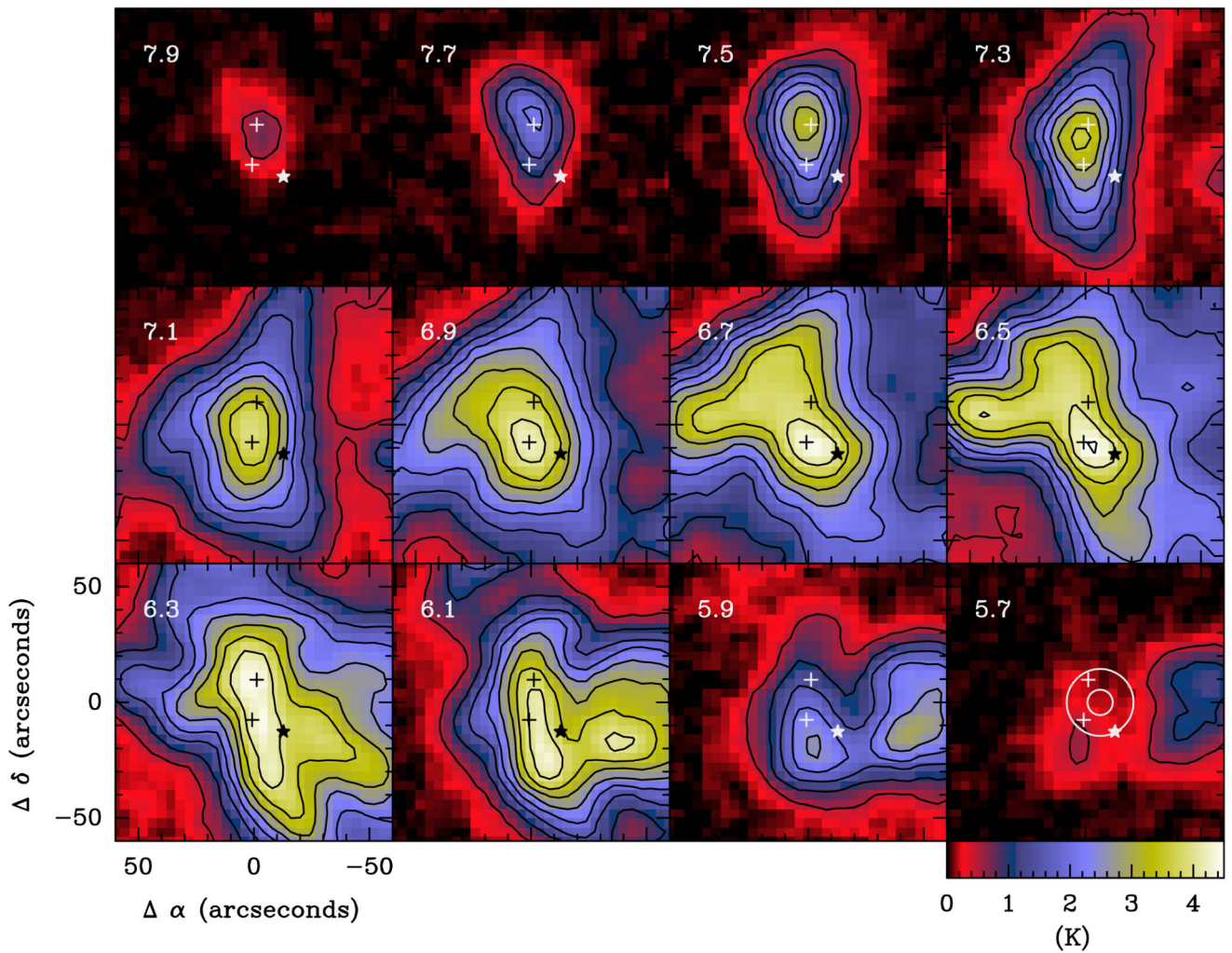


Fig. 4. Spectral maps of the $\text{DCO}^+ 2 \rightarrow 1$ line as observed with the IRAM 30m telescope. The central velocity is indicated in the top-left corner. Contours are 0.5 K to 4.5 K by steps of 0.5 K. The crosses mark the positions of the protostellar cores B1b-N and B1b-S. The star marks the position of B1b-W.

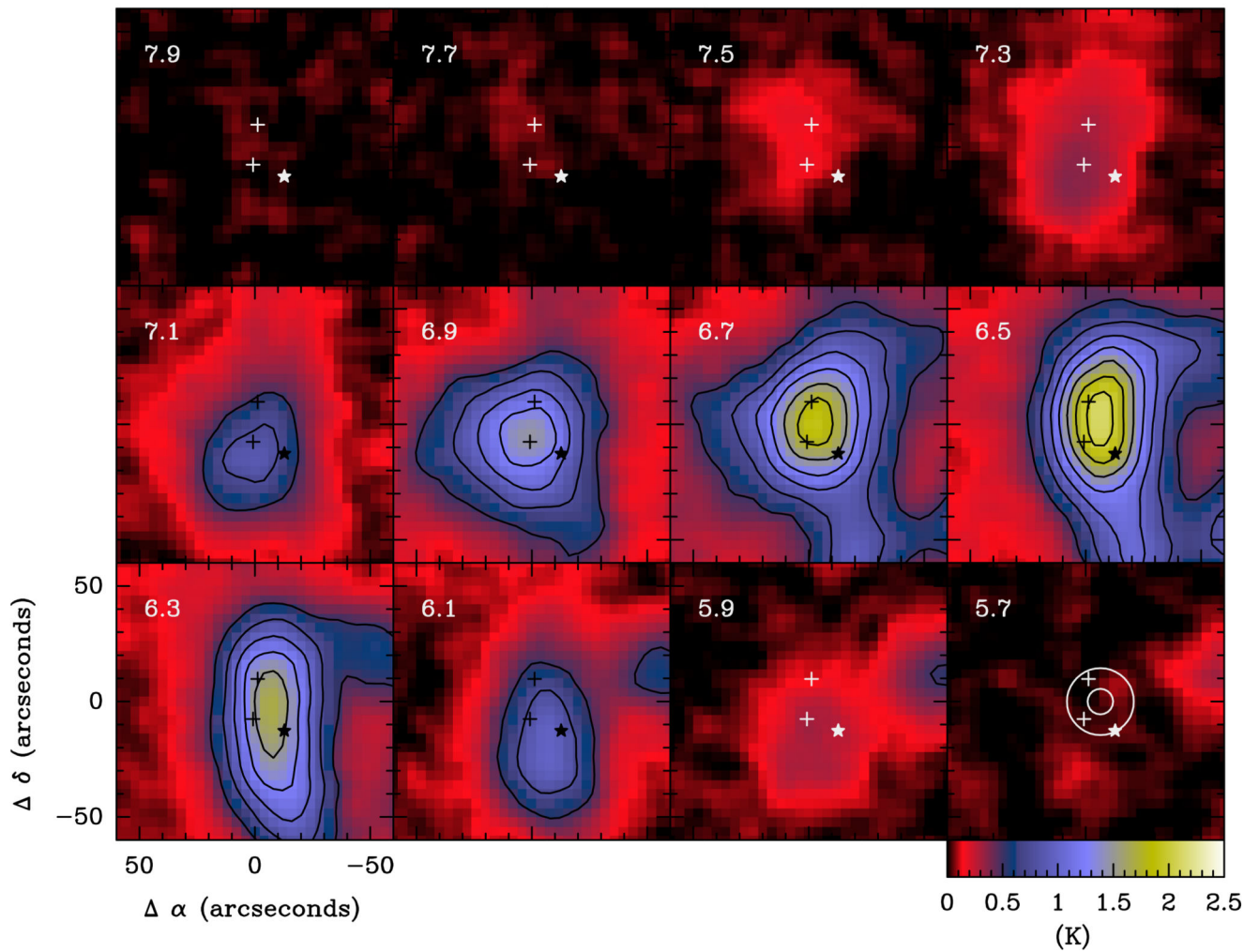


Fig. 5. Spectral maps of the $\text{SO } 2_2 \rightarrow 1_1$ line as observed with the IRAM 30m telescope. The central velocity is indicated in the top-left corner. Contours are 0.5 K to 4.5 K by steps of 0.25 K. The crosses mark the positions of the protostellar cores B1b-N and B1b-S. The star marks the position of B1b-W.

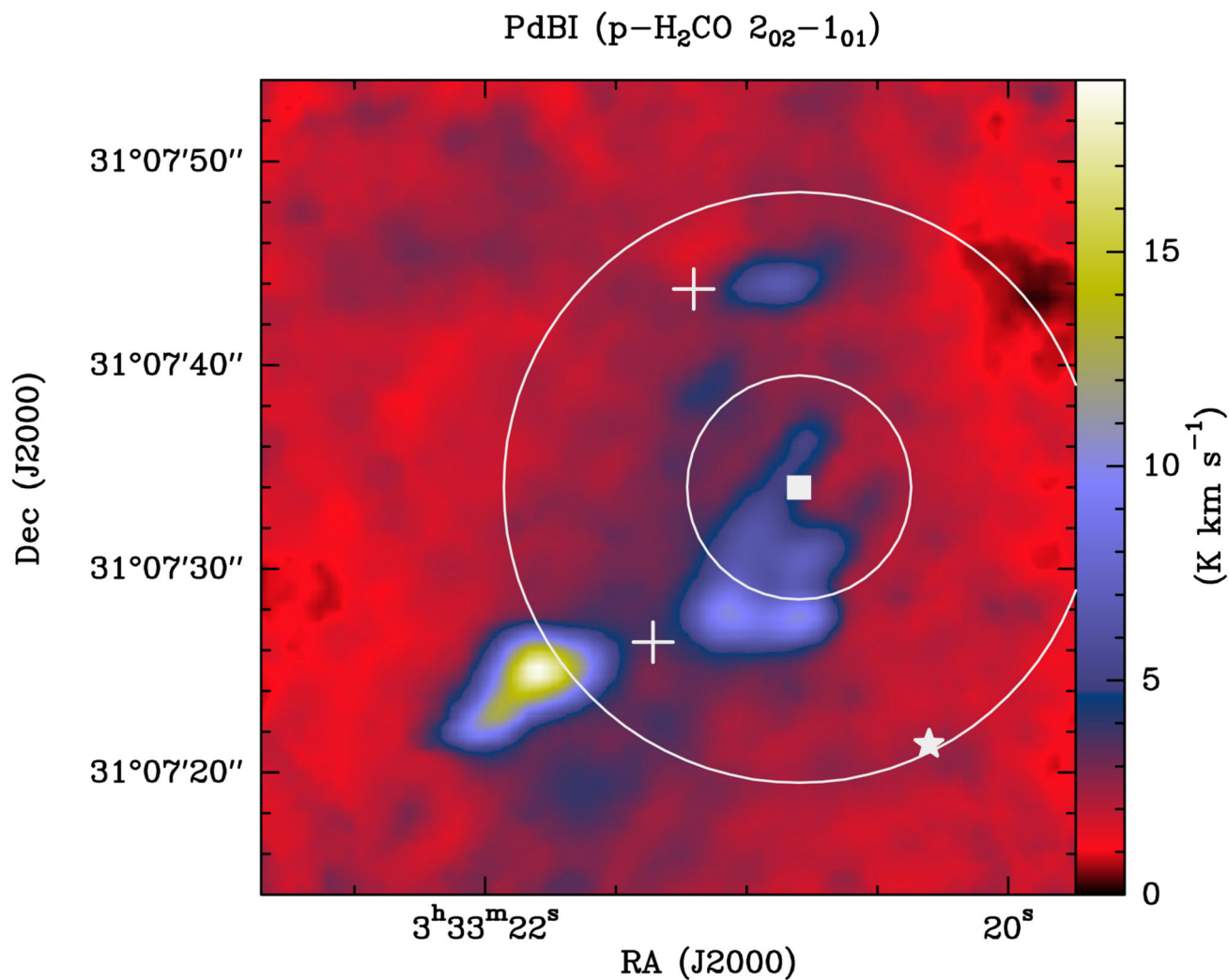


Fig. 6. Interferometric integrated intensity map of the outflows associated with B1b-N and B1b-S in the $\text{H}_2\text{CO } 2_{0,2}1_{0,1}$ line (Gerin et al., 2015). The crosses mark the positions of the protostellar cores B1b-N and B1b-S and the star, of B1b-W. The position targeted by our spectral survey is drawn with a white square and the beams of the 30m telescope at 3mm and 1mm are indicated by white circles.

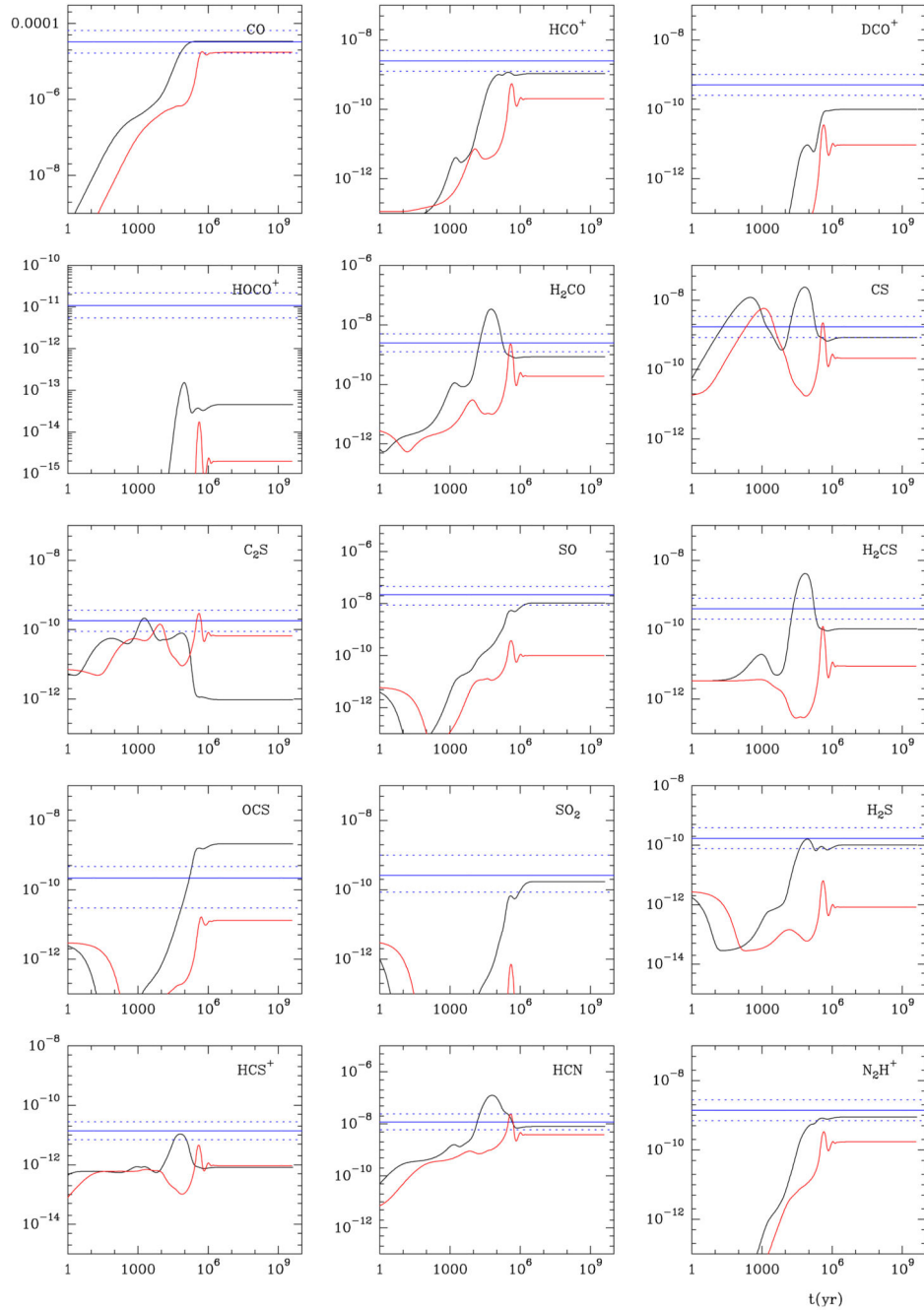


Fig. 7.

Results of our best fit model ($\zeta_{H_2}=4.0 \times 10^{-17} \text{ s}^{-1}$, $O/H=3.0 \cdot 10^{-5}$, $N/H=6.4 \cdot 10^{-5}$, $C/H=1.7 \cdot 10^{-5}$ and $S/H=6.0 \cdot 10^{-7}$). We assume a density of $n(H_2)=10^5 \text{ cm}^{-3}$ and $T_K=12 \text{ K}$. Thick and dashed blue lines indicate the observed values and their uncertainty, which is considered to be a factor of 2 for most molecules (see text), respectively. In the case of SO, SO₂ and OCS, their abundances change by more than a factor of 2 between the 6.5 km s⁻¹ and 7.0 km s⁻¹ velocity components. In the panels corresponding to these species, the dashed lines indicate

the abundance for each component separately. In red we show model calculations for the same conditions and $n(\text{H}_2)=10^4 \text{ cm}^{-3}$.

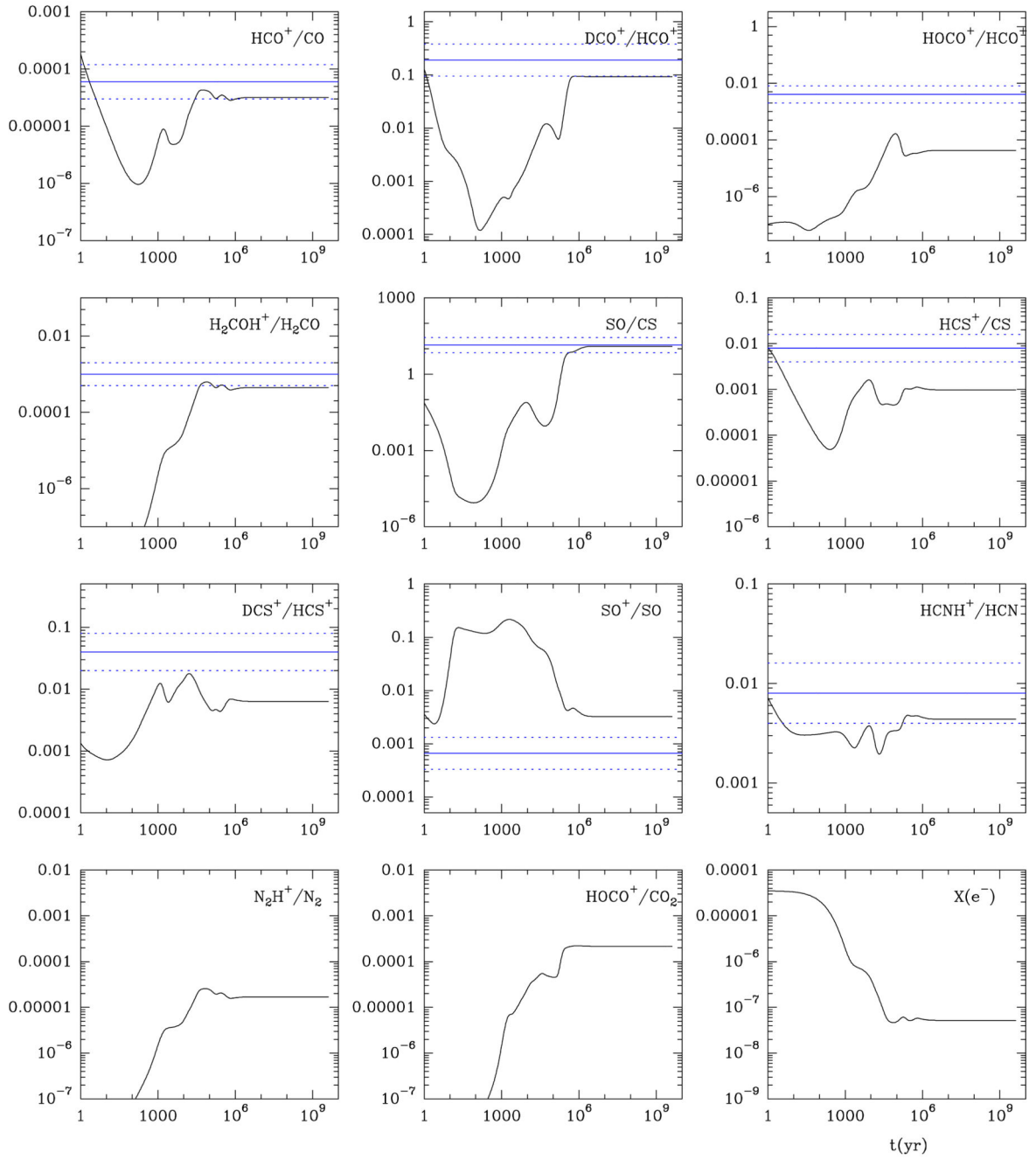
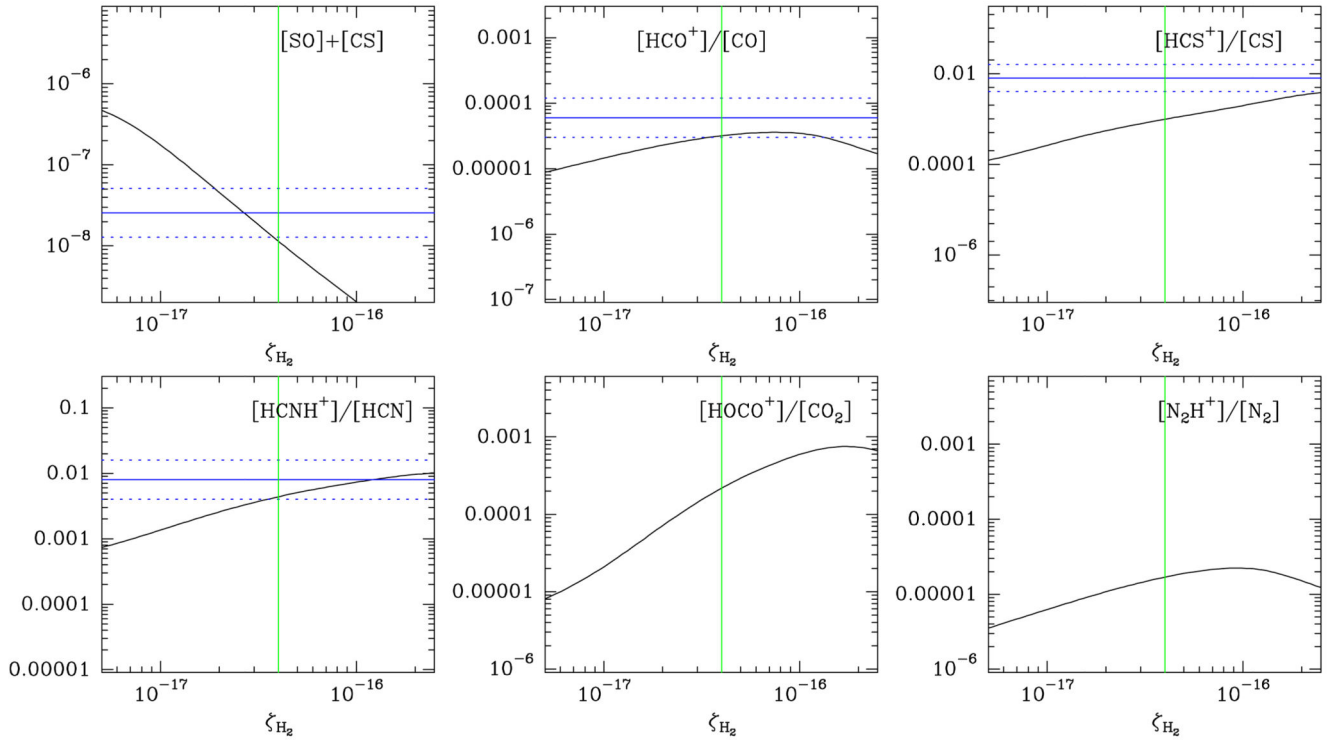


Fig. 8.

Results of our best fit model ($\zeta_{HD}=4.0\times 10^{-17} \text{ s}^{-1}$, $O/H=3.0 \cdot 10^{-5}$, $N/H=6.4 \cdot 10^{-5}$, $C/H=1.7 \cdot 10^{-5}$ and $S/H=6.0 \cdot 10^{-7}$). We assume a density of $n(\text{H}_2)=10^5 \text{ cm}^{-3}$ and $T_k=12 \text{ K}$. Thick and dashed blue lines indicate the observed values and their uncertainties.

**Fig. 9.**

Steady state calculations of fractional abundances and abundance ratios. All the input parameters except ζ_{H_2} are the same as in Fig. 7. Horizontal blue lines correspond to the observed values and their uncertainty that is considered a factor of 2. Vertical green lines indicate the estimated value of the cosmic ray ionization rate, $\zeta_{H_2} = 4 \times 10^{-17}$ s $^{-1}$.

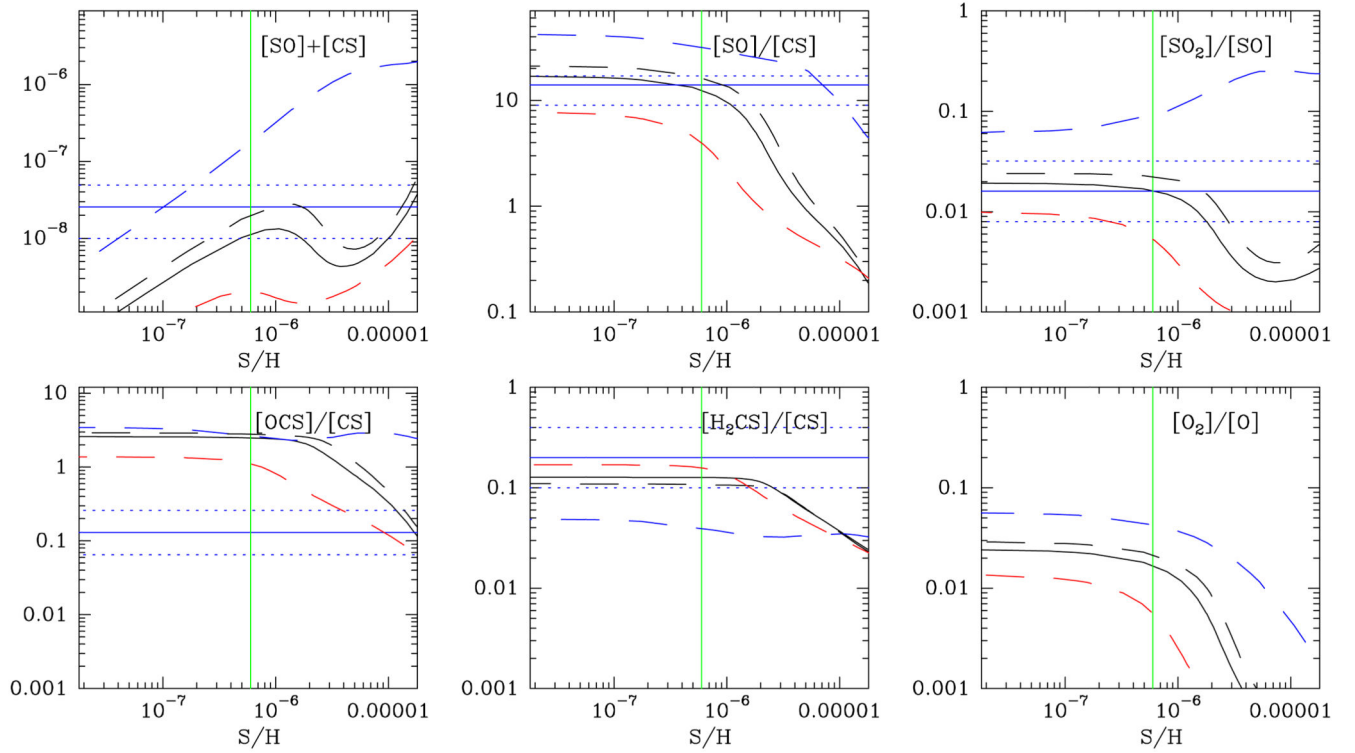
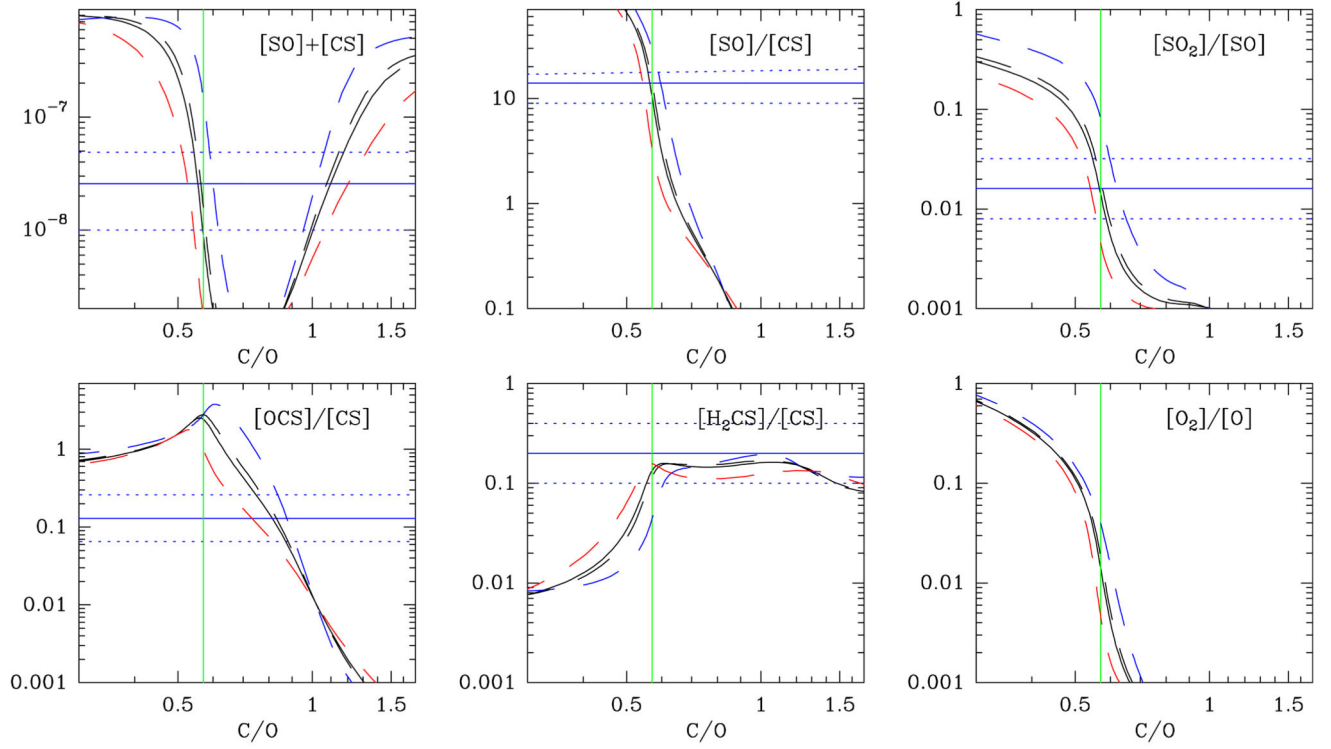


Fig. 10.

Steady state calculations of fractional abundances and abundance ratios. All the input parameters except S/H are the same as in Fig. 7. Horizontal blue lines correspond to the observed values and their uncertainty. Vertical green lines indicate the estimated value of the sulfur elemental abundance, $S/H=6\times 10^{-7}$. The solid black line is our best model fit, $\zeta_{H2}=4\times 10^{-17} \text{ s}^{-1}$. The dashed blue, black and red lines corresponds to $\zeta_{H2}=1, 4$ and $10\times 10^{-17} \text{ s}^{-1}$, respectively.

**Fig. 11.**

Steady state calculations of fractional abundances and abundance ratios. All the input parameters except O/H are the same as in Fig. 7. Horizontal blue lines correspond to the observed values and their uncertainty. Vertical green lines indicate the estimated value of C/O elemental ratio, $C/O=0.6$. The dashed blue, black and red lines corresponds to $\zeta_{H_2} = 1, 4$ and $10 \times 10^{-17} \text{ s}^{-1}$, respectively.

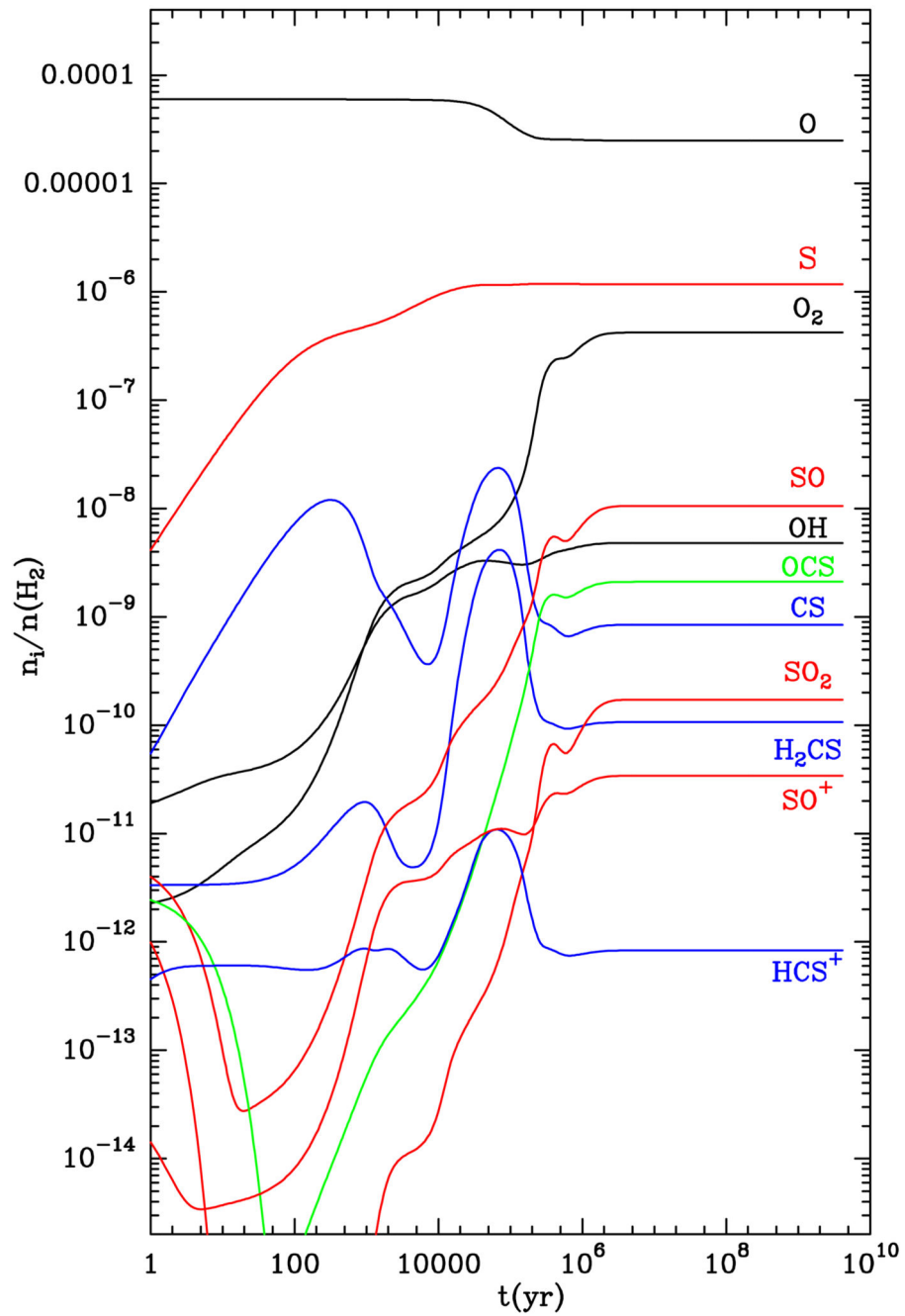


Fig. 12.

Predicted fractional abundances using the same parameters as in Fig 7. Note that the abundance of SO, SO₂ and SO⁺ and O₂ dramatically increase after 1 Myr.

Table 1

Observing and telescope parameters.

Freq (GHz)	v (km s⁻¹)	HPBW¹	B_{eff}	rms(T_a) (mK)
82.5–117.6	0.1255	29''–21''	0.81–0.78	3–5 ²
130.0–172.7	0.3424	19''–14''	0.74	6–10 ³
200.6–275.9	0.2839	12''–9''	0.63–0.49	5–10

¹HPBW(arcsec)≈2460/Freq(GHz);²rms~240 mK for v>114 GHz,;³rms~500 mK for v>169 GHz.

Table 2

Molecule	LTE				LVG ^f			
	6.5 km s ⁻¹	7.0 km s ⁻¹	Total	6.5 km s ⁻¹	7.0 km s ⁻¹	Total		
	T _{rot} (K)	N _X (cm ⁻²)	T _{rot} (K)	N _X (cm ⁻²)	N _X (cm ⁻²)	N _X (cm ⁻²)		
	<i>Ions</i>							
HC ¹⁸ O ⁺	4.4 ^{+0.2} _{-0.2}	1.7 ^{+0.1} _{-0.1} × 10 ¹¹	4.2 ^{+0.4} _{-0.7}	1.5 ^{+0.2} _{-0.3} × 10 ¹¹	3.2 × 10 ¹¹	2.0 ^{+0.1} _{-0.1} × 10 ¹¹	1.4 ^{+0.2} _{-0.3} × 10 ¹¹	3.4 × 10 ¹¹
D ¹³ CO ⁺	7.8 ^{+0.5} _{-0.5}	1.2 ^{+0.2} _{-0.2} × 10 ¹¹	4.5 ^{+0.2} _{-0.2}	3.9 ^{+0.5} _{-0.5} × 10 ¹¹	5.1 × 10 ¹¹	2.0 ^{+0.1} _{-0.1} × 10 ¹¹	4.5 ^{+0.1} _{-0.1} × 10 ¹¹	6.5 × 10 ¹¹
HOCO ⁺	11.9 ^{+0.3} _{-0.3}	5.2 ^{+0.3} _{-0.3} × 10 ¹¹	10.7 ^{+1.3} _{-1.0}	2.4 ^{+1.0} _{-0.7} × 10 ¹¹	7.6 × 10 ¹¹	5.2 ^{+0.2} _{-0.2} × 10 ¹¹	3.0 ^{+0.2} _{-0.2} × 10 ¹¹	8.2 × 10 ¹¹
DOCO ⁺	11 ^a	7.0 ^{+0.9} _{-0.9} × 10 ¹⁰	11 ^a	4.0 ^{+2.0} _{-2.0} × 10 ¹⁰	1.1 × 10 ¹¹	9.0 ^{+1.1} _{-1.1} × 10 ¹⁰	5.0 ^{+2.0} _{-2.0} × 10 ¹⁰	1.1 × 10 ¹¹
SO ⁺	9.0 ^{+0.8} _{-0.7}	7.6 ^{+2.0} _{-1.6} × 10 ¹¹	8.3 ^{+2.2} _{-1.4}	4.8 ^{+4.1} _{-2.2} × 10 ¹¹	1.2 × 10 ¹²			
HCS ⁺	10.6 ^{+6.5} _{-3.0}	2.1 ^{+3.6} _{-1.3} × 10 ¹¹	7.5 ^{+0.5} _{-0.6}	6.2 ^{+0.2} _{-0.2} × 10 ¹¹	8.3 × 10 ¹¹	5.5 ^{+0.1} _{-0.1} × 10 ¹¹	5.5 ^{+0.1} _{-0.1} × 10 ¹¹	1.1 × 10 ¹²
DCS ⁺	10 ^b	5.0 ^{+1.0} _{-1.0} × 10 ¹⁰			5.0 × 10 ¹⁰	4.5 ^{+1.1} _{-1.1} × 10 ¹⁰		4.5 × 10 ¹⁰
HCNH ⁺	29.0 ⁺⁵⁰ ₋₁₂	5.1 ^{+4.1} _{-0.7} × 10 ¹²	8.9 ^{+5.3} _{-2.9}	3.8 ^{+1.5} _{-0.5} × 10 ¹²	8.9 × 10 ¹²	3.7 ^{+0.4} _{-0.4} × 10 ¹²	4.0 ^{+0.4} _{-0.4} × 10 ¹²	7.7 × 10 ¹²
H ₂ COH ⁺			10 ^a	2.0 ^{+1.0} _{-1.0} × 10 ¹¹	2.0 ^{+1.0} _{-1.0} × 10 ¹¹			
CO ⁺			10 ^a	<6.0 × 10 ¹⁰	<6.0 × 10 ¹⁰			
HOC ⁺			10 ^a	<2.0 × 10 ¹⁰	<2.0 × 10 ¹⁰			
	<i>Neutrals</i>							
¹³ C ¹⁸ O	5.5 ^{+1.3} _{-0.9}	2.4 ^{+0.2} _{-0.2} × 10 ¹³	10.9 ^{+0.9} _{-1.4}	5.2 ^{+0.1} _{-0.1} × 10 ¹³	7.6 × 10 ¹³	3.0 ^{+0.2} _{-0.2} × 10 ¹³	6.0 ^{+0.3} _{-0.3} × 10 ¹³	9.0 × 10 ¹³
o-H ₂ ¹³ CO	5.5 ^{+0.8} _{-0.6}	6.1 ^{+2.1} _{-1.5} × 10 ¹¹	5.2 ^{+0.9} _{-0.3}	4.9 ^{+3.2} _{-1.9} × 10 ¹¹	1.1 × 10 ¹²	1.1 ^{+0.6} _{-0.6} × 10 ¹²	1.3 ^{+0.7} _{-0.7} × 10 ¹²	2.4 × 10 ¹²
¹³ CS	7.1 ^{+1.6} _{-1.1}	7.8 ^{+2.0} _{-5.7} × 10 ¹¹	3.2 ^{+0.4} _{-0.7}	3.1 ^{+3.2} _{-1.6} × 10 ¹²	3.9 × 10 ¹²	1.3 ^{+0.1} _{-0.1} × 10 ¹²	9.0 ^{+0.3} _{-0.3} × 10 ¹¹	2.2 ^{+0.1} _{-0.1} × 10 ¹²
S ¹⁸ O	6.8 ^{+0.6} _{-0.6}	1.6 ^{+0.6} _{-0.5} × 10 ¹²	8.2 ^{+2.0} _{-1.4}	0.6 ^{+0.4} _{-0.3} × 10 ¹²	2.3 × 10 ¹²	2.2 ^{+0.1} _{-0.1} × 10 ¹²	8.0 ^{+0.3} _{-0.3} × 10 ¹¹	3.0 × 10 ¹²

Molecule	LTE			LVG ^f		
	6.5 km s ⁻¹	7.0 km s ⁻¹	Total	6.5 km s ⁻¹	7.0 km s ⁻¹	Total
	$T_{rot}(K)$	$T_{rot}(K)$	$N_X(cm^{-2})$	$N_X(cm^{-2})$	$N_X(cm^{-2})$	$N_X(cm^{-2})$
³³ SO	12.3 ^{+7.3} _{-4.0}	18.9 ^{+7.1} _{-8.3}	0.7 ^{+0.7} _{-0.4} × 10 ¹²	3.8 ^{+0.1} _{-0.1} × 10 ¹²	6.0 ^{+2.0} _{-2.0} × 10 ¹¹	4.4 × 10 ¹²
³⁴ SO ₂	5.8 ^{+2.0} _{-1.2}		1.1 ^{+1.0} _{-0.5} × 10 ¹²	1.1 ^{+0.1} _{-0.1} × 10 ¹²		
SO ₂	10.1 ^{+1.0} _{-1.0}	10.2 ^{+2.0} _{-1.2}	2.9 ^{+1.3} _{-0.9} × 10 ¹²	1.6 ^{+0.1} _{-0.1} × 10 ¹³	4.5 ^{+0.1} _{-0.1} × 10 ¹²	2.0 × 10 ¹³
OC ³⁴ S	8.7 ^{+0.6} _{-0.5}		1.2 ^{+0.2} _{-0.2} × 10 ¹²	1.0 ^{+0.3} _{-0.3} × 10 ¹²		
OCS	11.7 ^{+13.0} _{-4.0}	20.4 ^{+1.4} _{-1.3}	4.9 ^{+0.6} _{-0.6} × 10 ¹²	1.7 ^{+0.1} _{-0.1} × 10 ¹³	8.0 ^{+4.0} _{-4.0} × 10 ¹¹	1.7 × 10 ¹³
H ₂ ¹³ CS ^c	7.4		1.6 ^{+0.3} _{-0.3} × 10 ¹¹			
CCS	8.3 ^{+0.7} _{-0.6}	8.2 ^{+0.7} _{-0.6}	5.9 ^{+2.4} _{-1.7} × 10 ¹²	9.3 ^{+0.1} _{-0.1} × 10 ¹²	5.2 ^{+0.1} _{-0.1} × 10 ¹²	1.4 × 10 ¹³
CC ³⁴ S				3.5 ^{+0.7} _{-0.7} × 10 ¹¹	2.5 ^{+0.7} _{-0.7} × 10 ¹¹	6.0 × 10 ¹¹
CCGS						
C ¹³ CCS						
o-H ₂ S	10 ^d	10	7.0 ^{+0.2} _{-0.2} × 10 ¹²	3.0 ^{+0.2} _{-0.2} × 10 ¹²		1.0 × 10 ¹³
NS	10 ^d	10	5.4 ^{+0.2} _{-0.2} × 10 ¹²	9.0 ^{+0.2} _{-0.2} × 10 ¹²		1.4 × 10 ¹³

^f LVG calculations assuming $T_K=12$ K and $n(H_2)=10^5$ cm⁻³;

^a Assuming the rotation temperature of HOCO⁺;

^b Assuming the rotation temperature of HCS⁺;

^c In this case the ortho and para species are treated together (ortho-to-para(OTP)=3) and we have assumed the rotation temperature calculated for H₂CS by Marcelino et al. (2005);

^d Reasonable guess for the rotation temperature.

Table 3

Fractional abundances and abundance ratios

Molecule	LTE			LVG ^I		
	6.5 km s ⁻¹	7.0 km s ⁻¹	Total	6.5 km s ⁻¹	7.0 km s ⁻¹	Total
	<i>Ions</i>			<i>Ions</i>		
X(HC ¹⁸ O ⁺)×550	3.9×10 ⁻⁹	1.8×10 ⁻⁹	2.5×10 ⁻⁹	4.6×10 ⁻⁹	1.7×10 ⁻⁹	2.7×10⁻⁹
X(D ¹³ CO ⁺)×60	2.7×10 ⁻¹⁰	4.7×10 ⁻¹⁰	4.0×10 ⁻¹⁰	4.6×10 ⁻¹⁰	5.4×10 ⁻¹⁰	5.1×10⁻¹⁰
X(HOCO ⁺)	2.0×10 ⁻¹¹	4.8×10 ⁻¹²	1.0×10 ⁻¹¹	2.0×10 ⁻¹¹	6.0×10 ⁻¹²	1.1×10⁻¹¹
X(DOCO ⁺)	2.9×10 ⁻¹²	8.0×10 ⁻¹³	1.4×10 ⁻¹²	3.6×10 ⁻¹²	1.0×10 ⁻¹²	1.4×10⁻¹²
X(SO ⁺)	3.1×10 ⁻¹¹	9.6×10 ⁻¹²	1.6×10⁻¹¹			
X(HCS ⁺)	8.1×10 ⁻¹²	1.2×10 ⁻¹¹	1.1×10 ⁻¹¹	2.1×10 ⁻¹¹	1.1×10 ⁻¹¹	1.4×10⁻¹¹
X(DCS ⁺)	1.9×10 ⁻¹²		6.6×10 ⁻¹³	1.7×10 ⁻¹²		5.9×10⁻¹³
X(HCNH ⁺)	2.0×10 ⁻¹⁰	7.6×10 ⁻¹¹	1.2×10 ⁻¹⁰	1.4×10 ⁻¹⁰	8.0×10 ⁻¹¹	1.0×10⁻¹⁰
X(H ₂ COH ⁺)		4.0×10 ⁻¹²	2.6×10⁻¹²			
X(CO ⁺)			<7.9×10 ⁻¹³			
X(HOC ⁺)			<2.6×10 ⁻¹³			
X(NNH ⁺)			1.4×10⁻⁹*			
X(NND ⁺)			5.0×10⁻¹⁰*			
	<i>Neutrals</i>			<i>Neutrals</i>		
X(¹³ C ¹⁸ O)	1.0×10 ⁻⁹	1.0×10 ⁻⁹	1.0×10 ⁻⁹	1.2×10 ⁻⁹	1.2×10 ⁻⁹	1.2×10⁻⁹
X(H ₂ ¹³ CO)×60 ^a	1.9×10 ⁻⁹	7.8×10 ⁻¹⁰	1.1×10 ⁻⁹	3.4×10 ⁻⁹	2.1×10 ⁻⁹	2.5×10⁻⁹
X(¹³ CS)×60	1.8×10 ⁻⁹	3.7×10 ⁻⁹	3.1×10 ⁻⁹	3.0×10 ⁻⁹	1.1×10 ⁻⁹	1.7×10⁻⁹
X(S ¹⁸ O)×550	3.7×10 ⁻⁸	6.3×10 ⁻⁹	1.8×10 ⁻⁸	5.0×10⁻⁸	9.0×10⁻⁹	2.2×10⁻⁸
X(³³ SO)×135	9.0×10 ⁻⁹	1.8×10 ⁻⁹	4.0×10 ⁻⁹	1.9×10 ⁻⁸	1.6×10 ⁻⁹	7.9×10 ⁻⁹
X(³⁴ SO ₂)×22.5	1.0×10 ⁻⁹			1.0×10 ⁻⁹		
X(SO ₂)	3.3×10 ⁻¹⁰	5.6×10 ⁻¹¹	1.4×10 ⁻¹⁰	6.7×10⁻¹⁰	9.0×10⁻¹¹	2.6×10⁻¹⁰
X(OC ³⁴ S)×22.5	1.1×10 ⁻⁹			9.4×10 ⁻¹⁰		
X(OCS)	6.2×10 ⁻¹⁰	9.4×10 ⁻¹¹	2.4×10 ⁻¹⁰	7.0×10⁻¹⁰	1.5×10⁻¹¹	2.2×10⁻¹⁰
X(H ₂ ¹³ CS)×60	4.0×10 ⁻¹⁰					
X(CCS)	2.4×10 ⁻¹⁰	6.9×10 ⁻¹¹	1.2×10 ⁻¹⁰	3.9×10 ⁻¹⁰	1.0×10 ⁻¹⁰	1.8×10⁻¹⁰
X(H ₂ S) ^a	3.9×10 ⁻¹⁰	7.7×10 ⁻¹¹	1.7×10⁻¹⁰			
X(NS)	2.2×10 ⁻¹⁰	1.7×10 ⁻¹⁰	1.8×10⁻¹⁰			
X(HCN)			1.2×10⁻⁸*			
	<i>Ion/Neutral and Ion/Ion</i>			<i>Ion/Neutral and Ion/Ion</i>		
$\frac{N(\text{HCO}^+)}{N(\text{CO})}$	1.1×10 ⁻⁴	4.8×10 ⁻⁵	6.9×10 ⁻⁵	1.1×10 ⁻⁴	4.3×10 ⁻⁵	6.8×10⁻⁵
$\frac{N(\text{DCO}^+)}{N(\text{HCO}^+)}$	0.07	0.26	0.15	0.1	0.32	0.19

Molecule	LTE			LVG ^I		
	6.5 km s ⁻¹	7.0 km s ⁻¹	Total	6.5 km s ⁻¹	7.0 km s ⁻¹	Total
$\frac{N(DCO^+)}{N(CO)}$	9.0×10 ⁻⁶	1.2×10 ⁻⁵	1.1×10 ⁻⁵	1.1×10 ⁻⁵	1.4×10 ⁻⁵	1.2×10⁻⁵
$\frac{N(HOCO^+)}{N(HCO^+)}$	0.005	0.003	0.004	0.004	0.003	0.004
$\frac{N(SO^+)}{N(SO)}$	8.0×10 ⁻⁴	0.0014	9.5×10⁻⁴			
$\frac{N(HCS^+)}{N(CS)}$	0.004	0.003	0.0035	0.007	0.01	0.008
$\frac{N(DCS^+)}{N(HSC^+)}$	0.24		0.06	0.08		0.04
$\frac{N(HCS^+)}{N(HCO^+)}$	0.003	0.007	0.004	0.004	0.006	0.005
$\frac{N(HCNH^+)}{N(HCN)}$			0.01			0.008
$\frac{N(H_2COH^+)}{N(H_2CO)}$		0.005	0.002			
$\frac{N(CO^+)}{N(HCO^+)}$			<3×10 ⁻⁴			
$\frac{N(HOC^+)}{N(HCO^+)}$			<1×10 ⁻⁴			
	<i>Neutral/Neutral</i>			<i>Neutral/Neutral</i>		
$\frac{N(SO)}{N(CS)}$	19	1.8	5	17	8	13
$\frac{N(SO_2)}{N(SO)}$	0.03	0.008	0.008	0.01	0.009	0.01
$\frac{N(CCS)}{N(CS)}$	0.13	0.02	0.04	0.12	0.09	0.11
$\frac{N(H_2CS)}{N(CS)}$	0.20					
$\frac{N(OCS)}{N(CS)}$	0.57	0.03	0.08	0.22	0.01	0.13

^I LVG calculations assuming $T_K=12$ K and $n(H_2)=10^5$ cm⁻³; numbers in boldface are used in Fig. 7 to Fig. 11 to compare with observations.

* From Daniel et al. (2013);

^a From Table 2 assuming OTP=3.

Table 4

Elemental abundances relative to H

	Solar		Dark cloud: TMC1 ¹		Barnard 1b ²	
	X/H ³	f _D ⁴	X/H	f _D	X/H	f _D
C	1.4 10 ⁻⁴	~1	1.4 10 ⁻⁴	~1	1.7 10 ⁻⁵	~8
O	3.1 10 ⁻⁴	~1	1.3 10 ⁻⁴	~2	3.0 10 ⁻⁵	~10
N	7.7 10 ⁻⁵	~1	6.2 10 ⁻⁵	~1	6.4 10 ⁻⁵	~1
S	1.5 10 ⁻⁵	~1	8.0 10 ⁻⁸	~200	6.0 10 ⁻⁷	~25

¹From the compilation by Agúndez & Wakelam (2013);²This work;³Elemental abundance in gas phase;⁴Depletion factor = (X/H)_⊙/(X/H).